Magnetic field reconstruction and power estimation: theory & extension to multipoint, multiscale missions

Schulz et al 2026 JGR

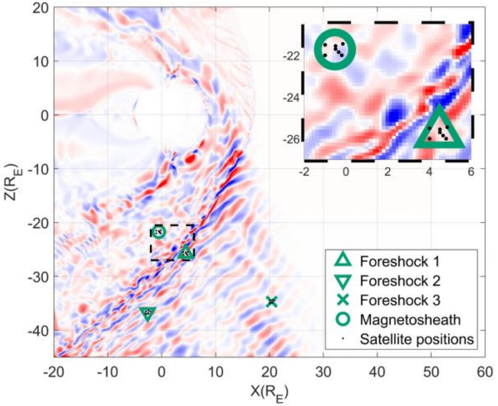

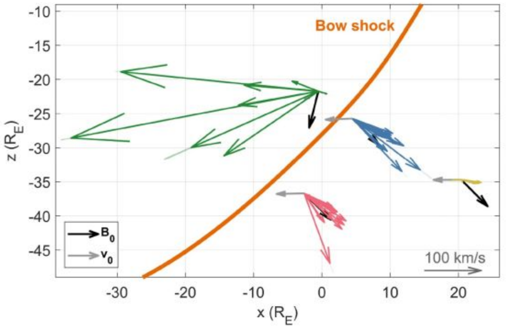

Broeren et al 2024 EASS

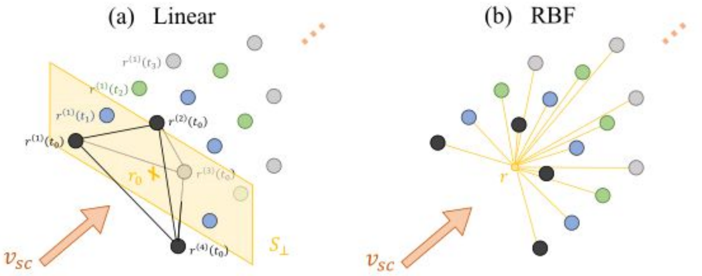

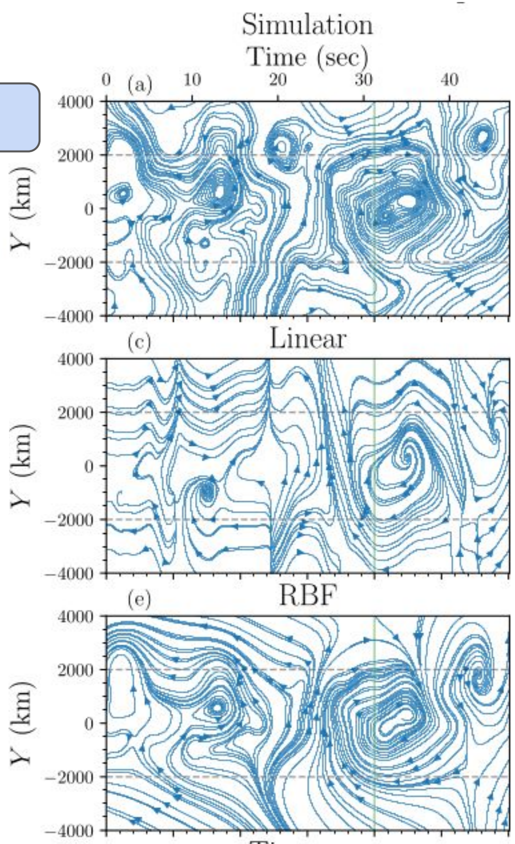

Kristopher Klein
University of Arizona

May 22, 2026

A Fundamental Limitation of Multipoint Observatories

For the foreseeable future, spatial coverage of spacecraft measurements will be sparse throughout some volume, given technical and financial limitations.

Given these constraints, we want to develop methods for characterizing the spatial and spectral distribution of power throughout the volume, and not just at the N-measurement points.

Arzamasskiy et al 2023 PRX

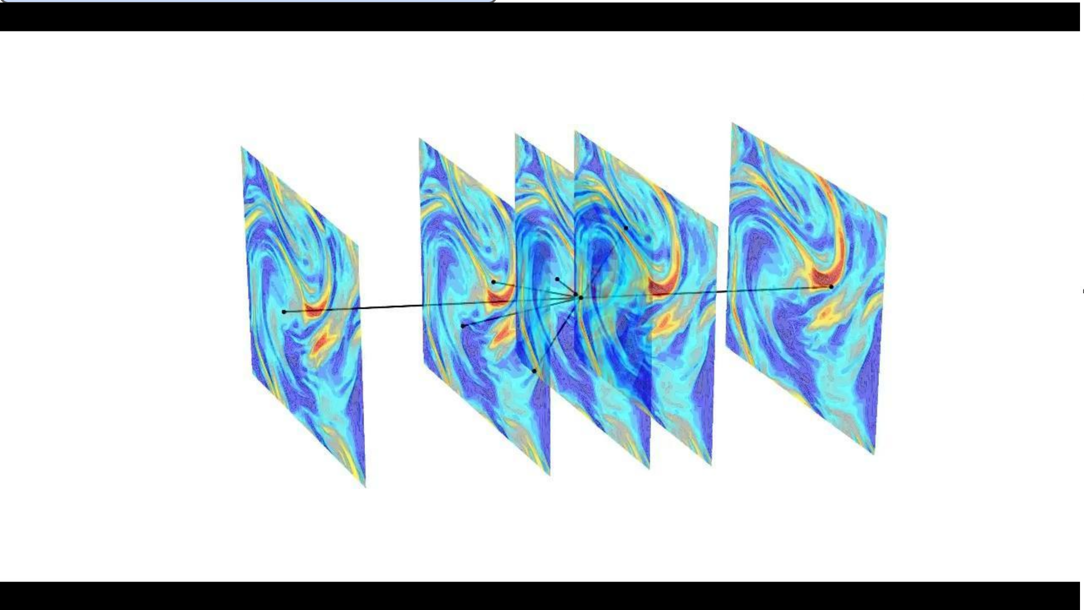

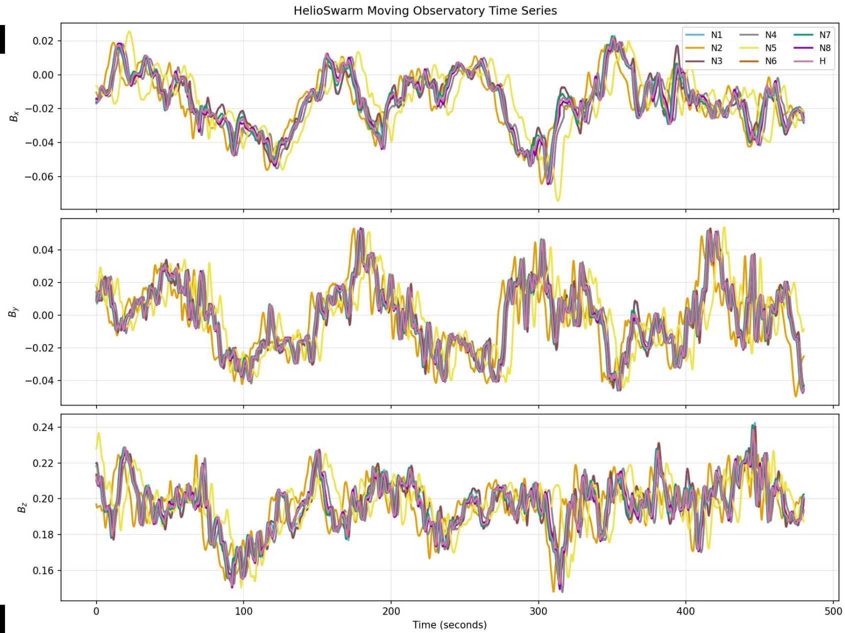

Two Complementary Methods for Multi Scale Observatories

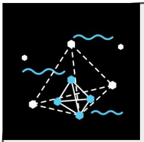

The **Wave Telescope** technique identifies the strongest waves present in a plasma by searching for maxima in the field energy density P(ω,**k**).

The measurement temporal cadence is sufficient to perform a frequency Fourier Transform, but spatial resolution is insufficient to approximate the sum.

We thus construct a spatial correlation matrix, and through a filter bank approach, estimate the spectral power. Narita et al 2022 provides a detailed overview and history of the technique.

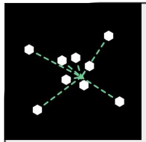

More general **Field Reconstruction** methods attempt to estimate the value of a vector field at spatial points with no local measurements.

This reconstruction is based on either physical arguments, e.g. known governing equations, or unphysical basis functions. Sec. 2 of Broeren et al 2024 provides references to many of these methods.

Both methods seek to reconstruct the distribution of some physical quantity from a sparse set of measurements

We will focus on extending these techniques to more than four measurement points

Coherent Waves are Abundant in the Heliosphere

Coherent waves with frequencies similar to the proton gyroradius are seen in about 30% of PSP observations (c.f. Bowen et al 2020 ApJ, W Liu et al 2023 ApJ) and are seen at 1 au in the solar wind (e.g. Jian et al 2009, Gary et al 2016) and Earth's foreshock (e.g. Wilson et al 2014a,b) continuously.

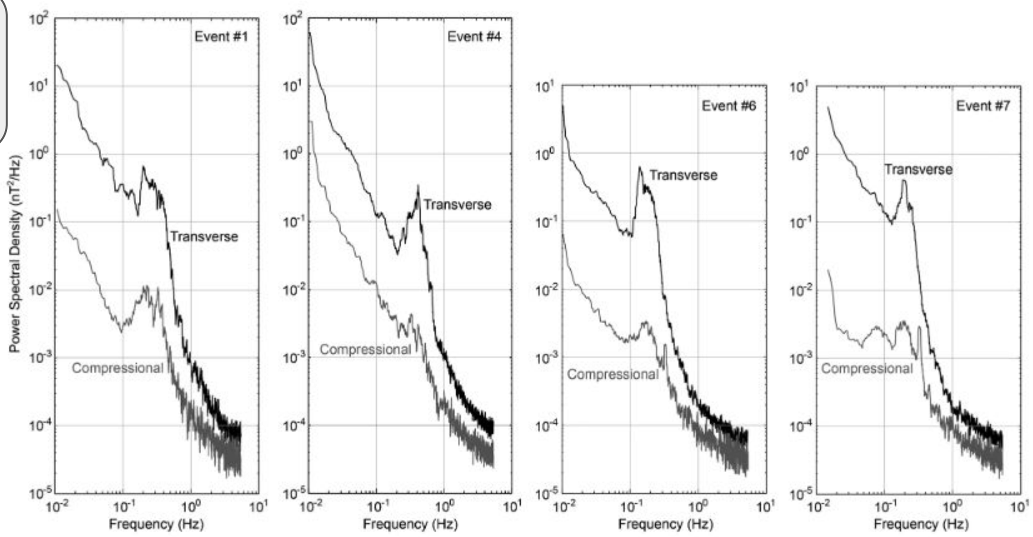

Gary et al 2016

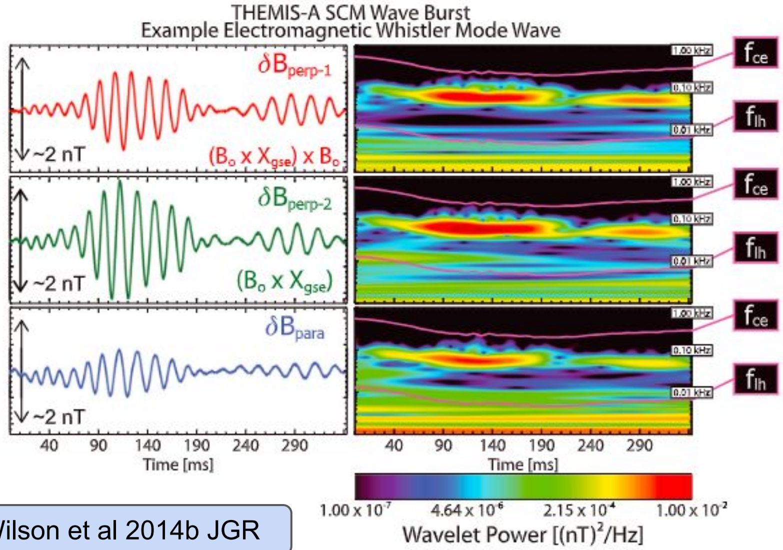

Wilson et al 2014b JGR

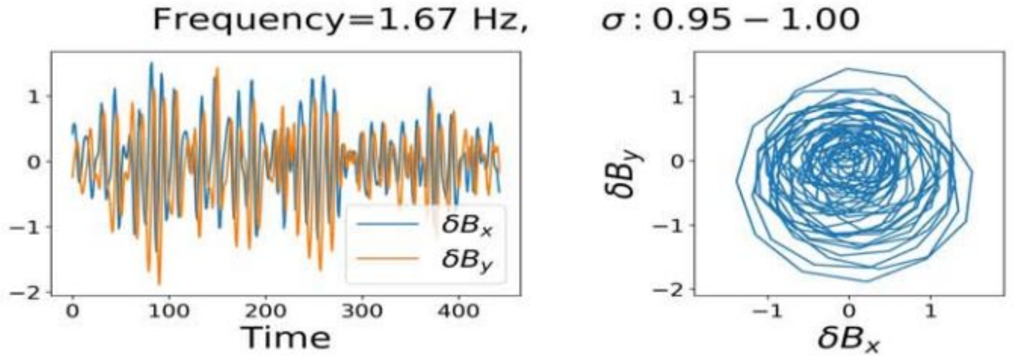

Niranjana et al 2023

PSP Observes Ion-Scale Waves Ubiquitously

Coherent waves with frequencies similar to the proton gyroradius are seen in about 30% of PSP observations (c.f. Bowen et al 2020 ApJ, W Liu et al 2023 ApJ) and are seen at 1 au in the solar wind (e.g. Jian et al 2009) and Earth's foreshock (Wilson et al 2014a,b) continuously.

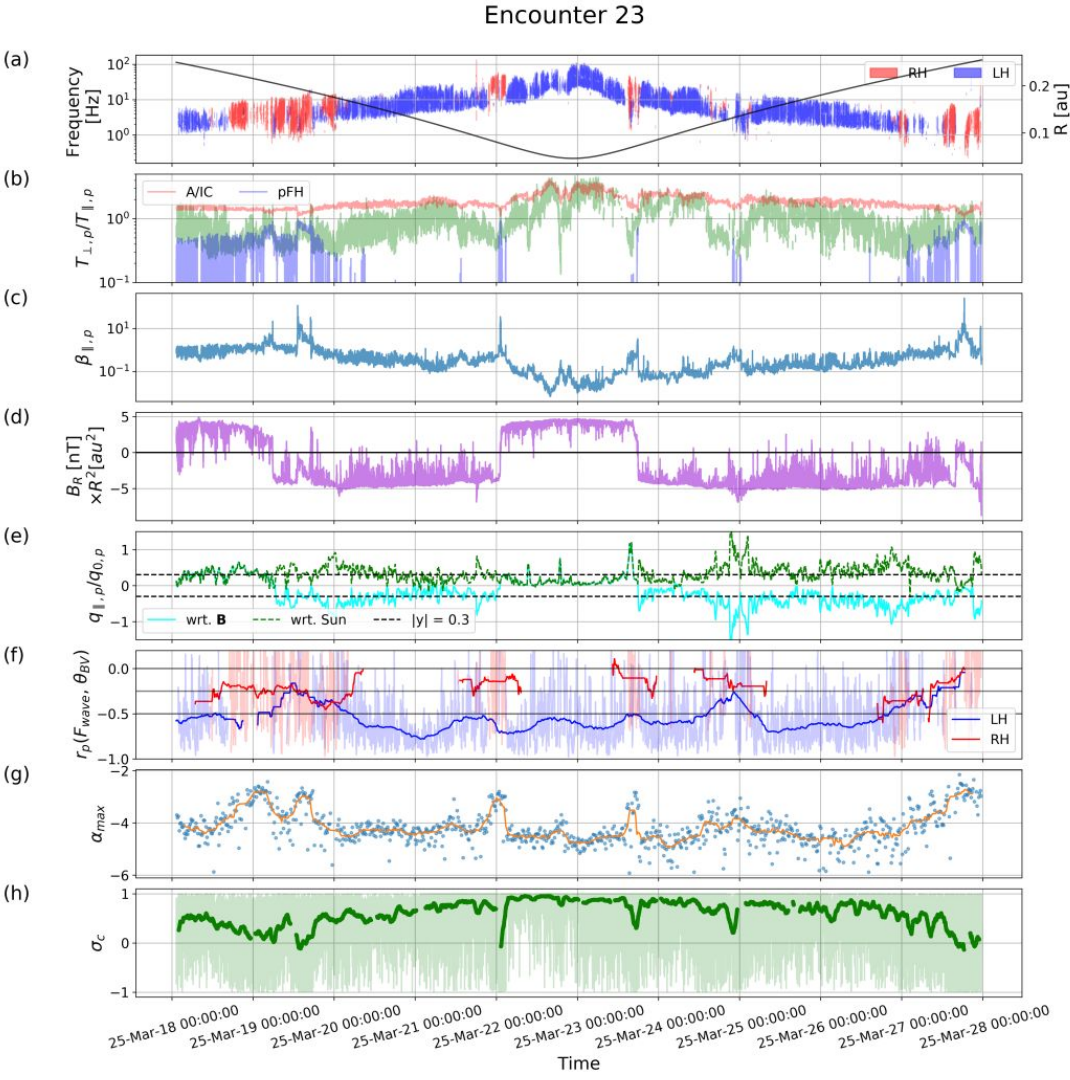

Free Energy Sources of Ion-scale Waves Observed by Parker Solar Probe; Niranjana 2026

PSP Ion-scale Circularly Polarized Wave Repository https://zenodo.org/records/17539353

Single-Point Measurements can not Disentangle Space and Time

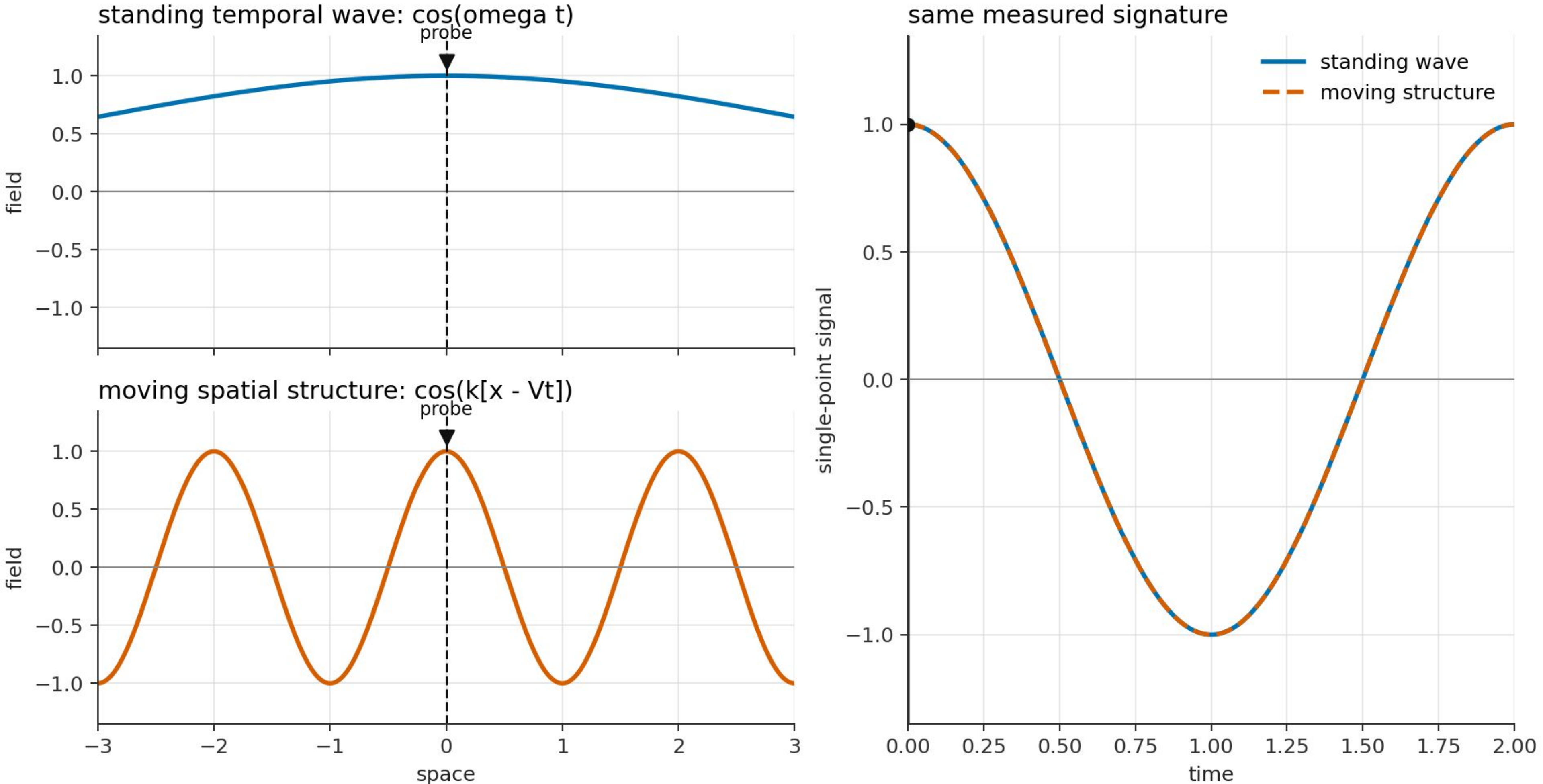

A Second Measurement Point Disentangles Space and Time

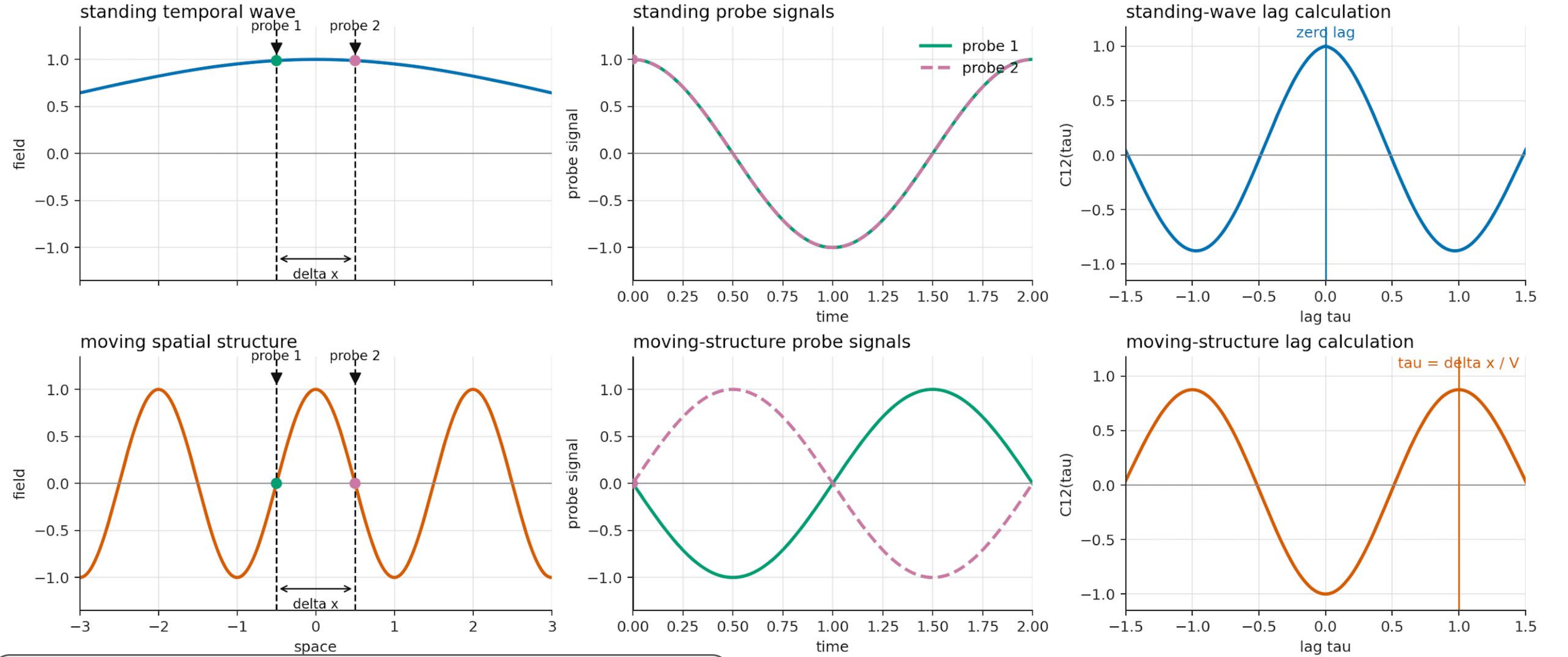

The lag correlation enables a determination of the spatial structure

$$C_{1,2}(\tau) = \langle F_1(t) F_2(t+\tau) \rangle$$

Better Constraints with More Measurements

With *many* points, we can more robustly extract the size of advected structures.

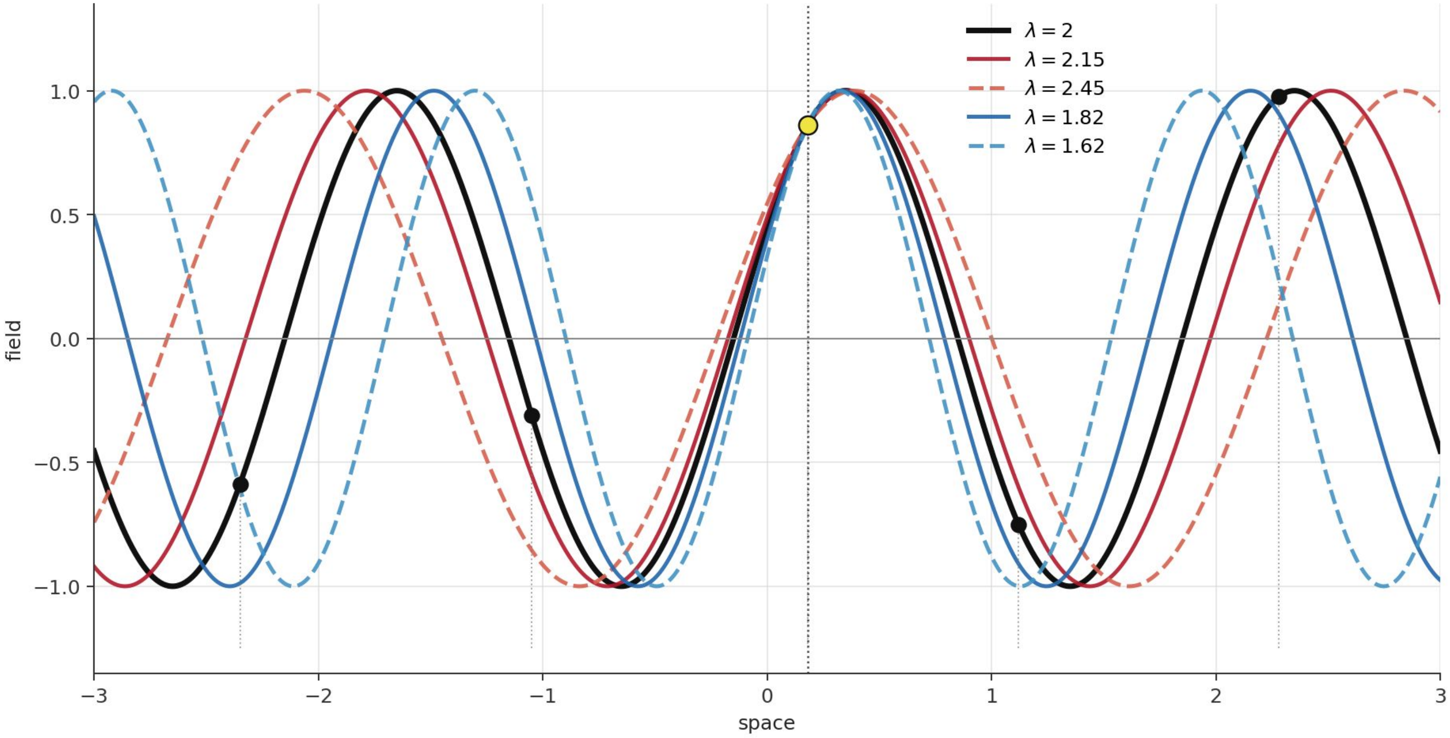

Our goal will be to generalize this to three dimensions and multiple waves.

Defining the Observatory Geometry

We can quantify polyhedral shapes using the volumetric tensor

$$R_{jk} = \frac{1}{N}\sum_{\alpha=1}^{N}(r_{\alpha,j} - r_{0,j})(r_{\alpha,k} - r_{0,k})$$

$$= \frac{1}{N}\sum_{\alpha=1}^{N}(r_{\alpha,j} r_{\alpha,k}) - r_{0,j} r_{0,k}$$

The associated eigenvalues quantify the shape's size L, elongation E, and planarity P.

These definitions generalize to N>4.

$$a = \sqrt{R^{(1)}}$$
$$\geq b = \sqrt{R^{(2)}}$$
$$\geq c = \sqrt{R^{(3)}}$$

$$L = 2a;$$

$$E = 1 - \frac{b}{a};$$

$$P = 1 - \frac{c}{b}$$

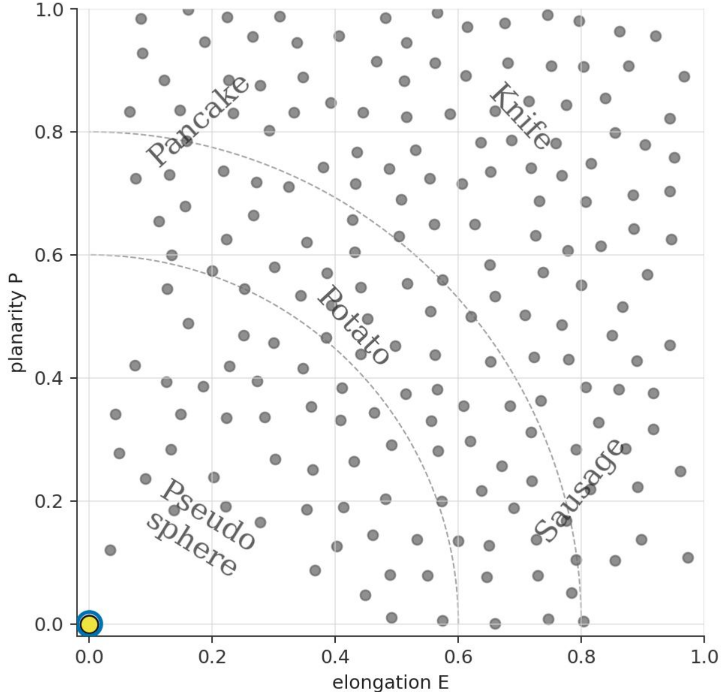

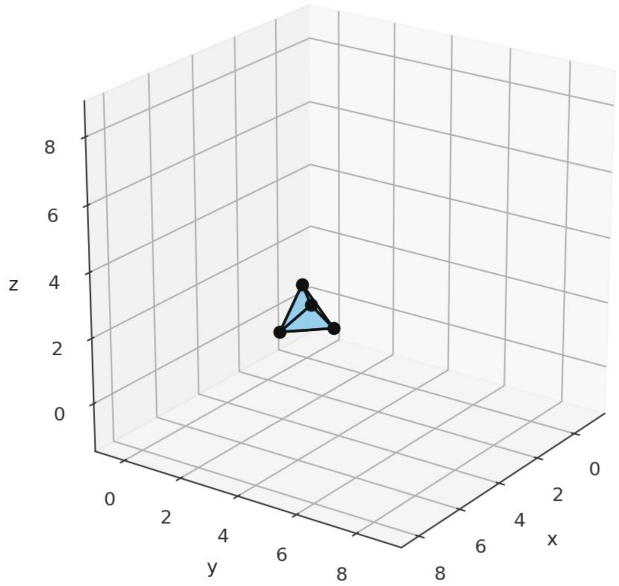

For later reference, we define

$$\chi = \sqrt{E^2 + P^2}$$

See *Tetrahedron Geometric Factors* Robert et al (Chapter 13 of Paschmann and Daly 1998)

Representing the Power Spectral Density

We begin assuming that the field can be expressed as a superposition of one's favorite* basis functions:

$$\mathbf{b}(t, \mathbf{r}^{(n)}) = \sum_{\omega} \sum_{\mathbf{k}} \mathbf{b}(\omega, \mathbf{k}) e^{i(\mathbf{k}\cdot\mathbf{r}^{(n)} - \omega t)}$$

and would like to calculate the spectral field energy density

$$P(\omega, \mathbf{k}) = \langle \mathbf{b}(\omega, \mathbf{k}) \mathbf{b}^{\dagger}(\omega, \mathbf{k}) \rangle$$

Given the dense temporal measurements, the time-to-frequency Fourier transform is easily performed, producing

$$\mathbf{b}(\omega, \mathbf{r}^{(n)}) = \frac{1}{2\pi} \sum_{t} \mathbf{b}(t, \mathbf{r}^{(n)}) e^{i\omega t} \longrightarrow \mathbf{b}(\omega, \mathbf{r}^{(n)}) = \sum_{\mathbf{k}} \mathbf{b}(\omega, \mathbf{k}) e^{i(\mathbf{k}\cdot\mathbf{r}^{(n)})}$$

Unfortunately, our measurements in **r** are not dense enough to approximate the complementary spatial-to-wavector sum. **We must therefore develop a different method.**

*Plane waves are most commonly used , but other functions can be invoked (c.f. Constantinescu et al., 2006, Plaschke et al., 2008).

Estimating the Power Spectral Density

Given our set of N time-to-frequency transformed measurements:

$$\tilde{\mathbf{b}}(\omega) = \begin{pmatrix} \mathbf{b}(\omega, \mathbf{r}^{(1)}) \\ \vdots \\ \mathbf{b}(\omega, \mathbf{r}^{(N)}) \end{pmatrix}_{3N\times 1} = \sum_{\mathbf{k}} \mathbf{H}(\mathbf{k})\mathbf{b}(\omega, \mathbf{k}) \ni \mathbf{H}(\mathbf{k}) = \begin{pmatrix} \mathbf{I}e^{i\mathbf{k}\cdot\mathbf{r}^{(1)}} \\ \vdots \\ \mathbf{I}e^{i\mathbf{k}\cdot\mathbf{r}^{(N)}} \end{pmatrix}$$

We define the **spatial correlation matrix**:

$$\mathbf{M}(\omega) = \frac{1}{Q}\sum_{q=1}^{Q} \left\langle \tilde{\mathbf{b}}_q(\omega)\tilde{\mathbf{b}}_q^{\dagger}(\omega) \right\rangle$$

and want a method for estimating **P**(ω,**k**) given our measured **M**(ω). Using some straightforward L.A tricks:

$$\mathbf{M}(\omega) = \sum_{\mathbf{k}} \mathbf{H}(\mathbf{k})\mathbf{P}(\omega, \mathbf{k})\mathbf{H}^{\dagger}(\mathbf{k})$$

The objective now is to find the matrix **P** which satisfies for all computed values of **M**(ω) and **H**(k).
We cannot directly invert this expression to solve for P because of the summation over k.
We will instead use a **filter-bank approach** to find a solution

A Choice of Weights

Our filter must relate our desired spectral field necessary for **P**(ω,**k**) to the measured fields, as

$$\mathbf{b}(\omega, \mathbf{k}) = \mathbf{W}^{\dagger}(\omega, \mathbf{k})\tilde{\mathbf{b}}(\omega)$$

Returning to our definitions, we can use these filters to relate

$$\mathbf{P}(\omega, \mathbf{k}) = \mathbf{W}^{\dagger}(\omega, \mathbf{k})\mathbf{M}(\omega)\mathbf{W}(\omega, \mathbf{k})$$

A few more lines of algebra and some Lagrange multipliers yields…

$$P(\omega, \mathbf{k}) = \mathrm{Tr}[\mathbf{H}^{\dagger}(\mathbf{k})\mathbf{M}^{-1}(\omega)\mathbf{H}(\mathbf{k})]^{-1}$$

Assuming we can invert **M** and know where our measurements are located, we can estimate P(**k**).

4 S/C Implementation

Motschmann et al 2006 (synthetic data)

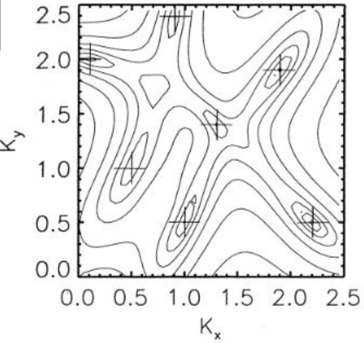

This method can be used to extract multiple wavevectors at a given frequency

Narita et al 2004

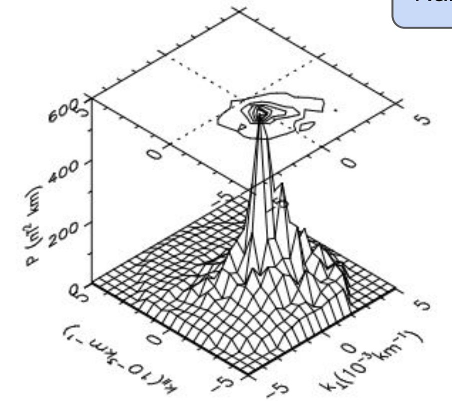

Cluster, 18 February 2002, 0805 – 0840 UT, 44.9 mHz

MMS and Cluster have enable the identification and quantification of waves in the magnetosphere, foreshock and the near-Earth Solar Wind

Narita and Glassmeier 2005

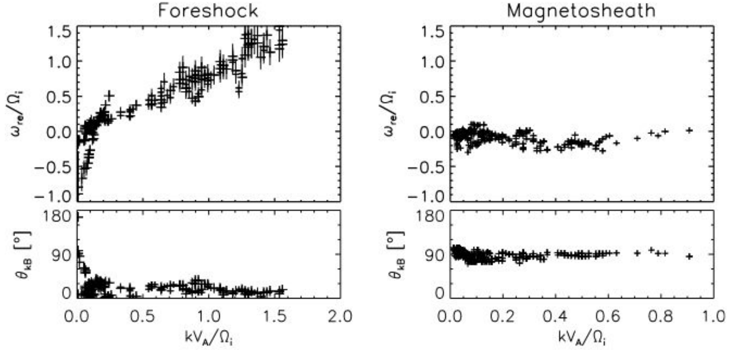

Phase speeds agree well with the expectation for Alfven waves

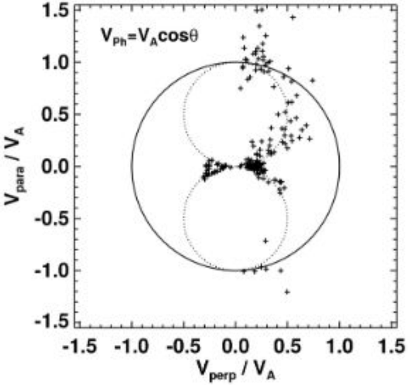

Schäfer et al 2005

Limitations with Four Spacecraft

The WT method is only sensitive to a limited range of wavevectors, covering a decade from the spacecraft separation to 10x larger.

Smaller waves are aliased, and larger waves are inaccurately characterized.

Broeren and Klein 2023

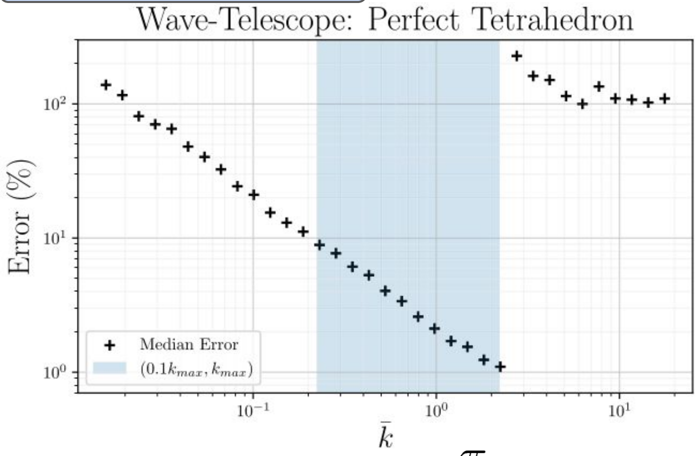

$$\bar{k} = kL,\ k_{\max} = \frac{\pi}{d_{\max}}$$

Given these wavevector limitations, there are also limitations on the frequencies that can be resolved with four spacecraft.

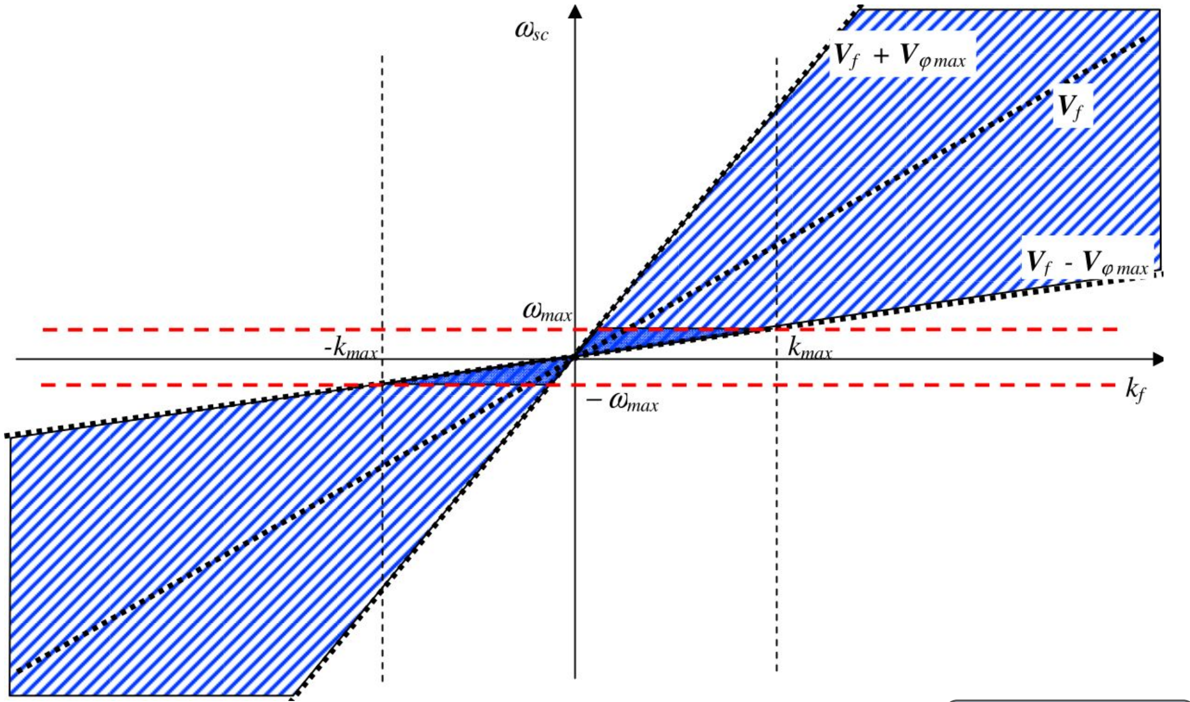

Sahraoui et al 2010 JGR

Aliasing becomes complex for N>4

Aliasing for irregularly spaced measurement points requires solving a NP problem; in position space, we want to find the shortest possible basis of the superlattice formed by the vectors of the spacecraft distances.

Determining the aliasing box can be attacked using a modified Lenstra–Lenstra–Lovàsz algorithm.

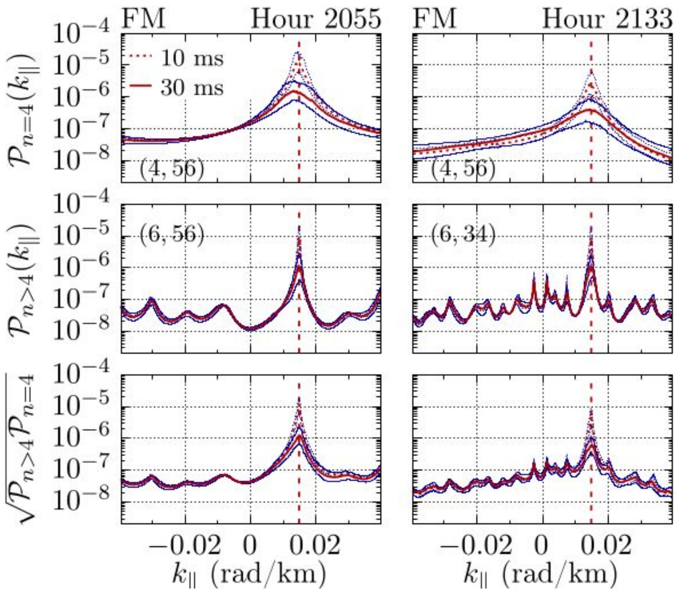

Klein et al 2024 JGR

See also Schulz et al 2026 JGR for a more sophisticated filtering method.

Schulz et al 2023 A&A

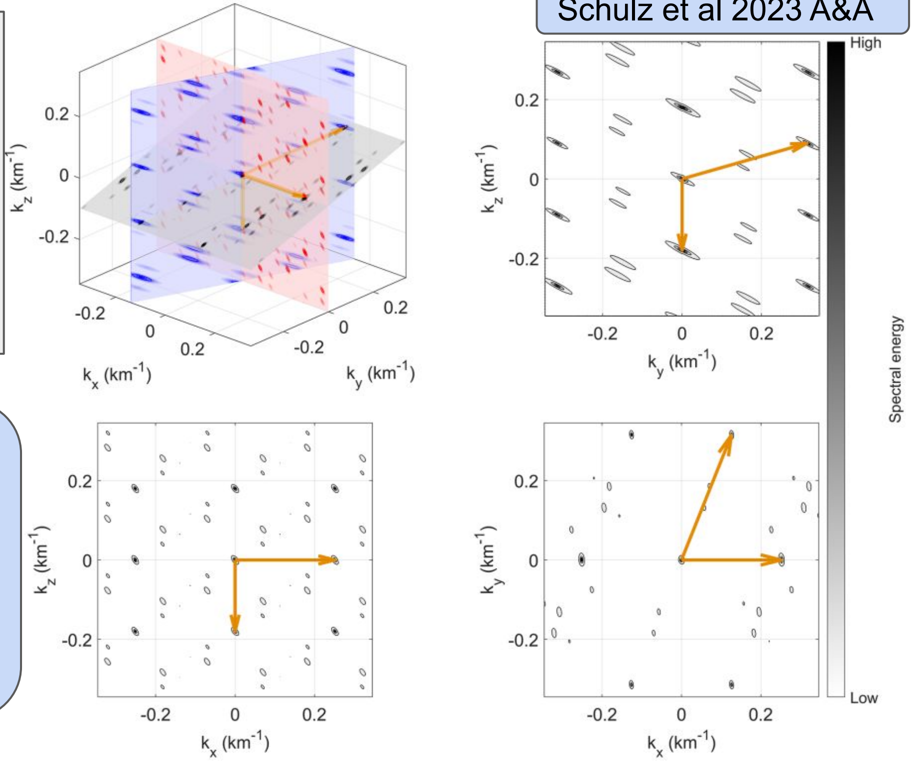

Combining polyhedra with different aliasing boxes can be used to reduce unphysical signals from individual WT applications.

Data-driven Uncertainty Quantification of the Wave Telescope Technique: General Equations and Demonstration Using HelioSwarm

We seek the error in the measured wavevector for arbitrary configurations with N spacecraft.

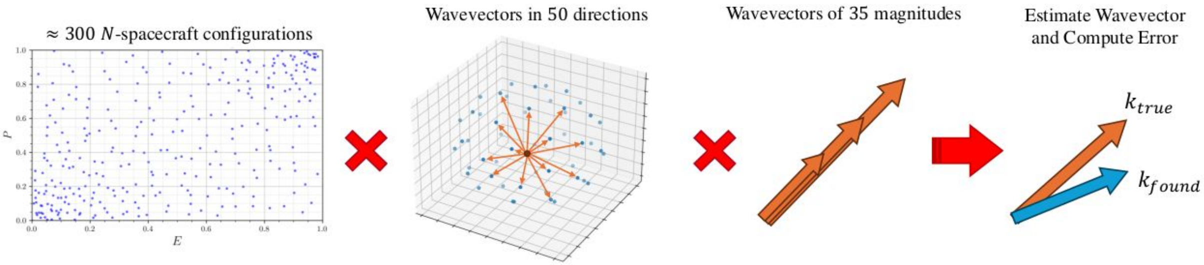

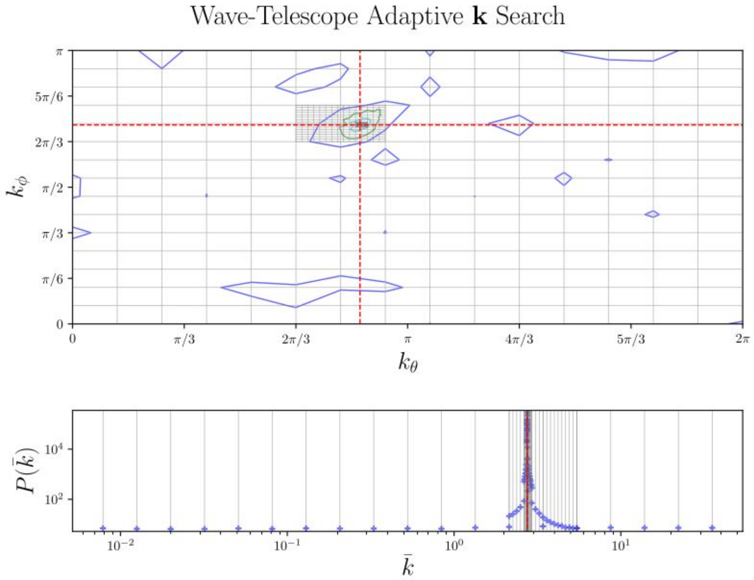

We construct hundreds of random configurations with uniformly varying \chi with N \in [4,9].

Broeren and Klein 2023

Learning Error via Bayesian Inference:

This produces a distribution of average errors, standard deviations of the errors, and a probability of aliasing as a function of N, k, and \chi:

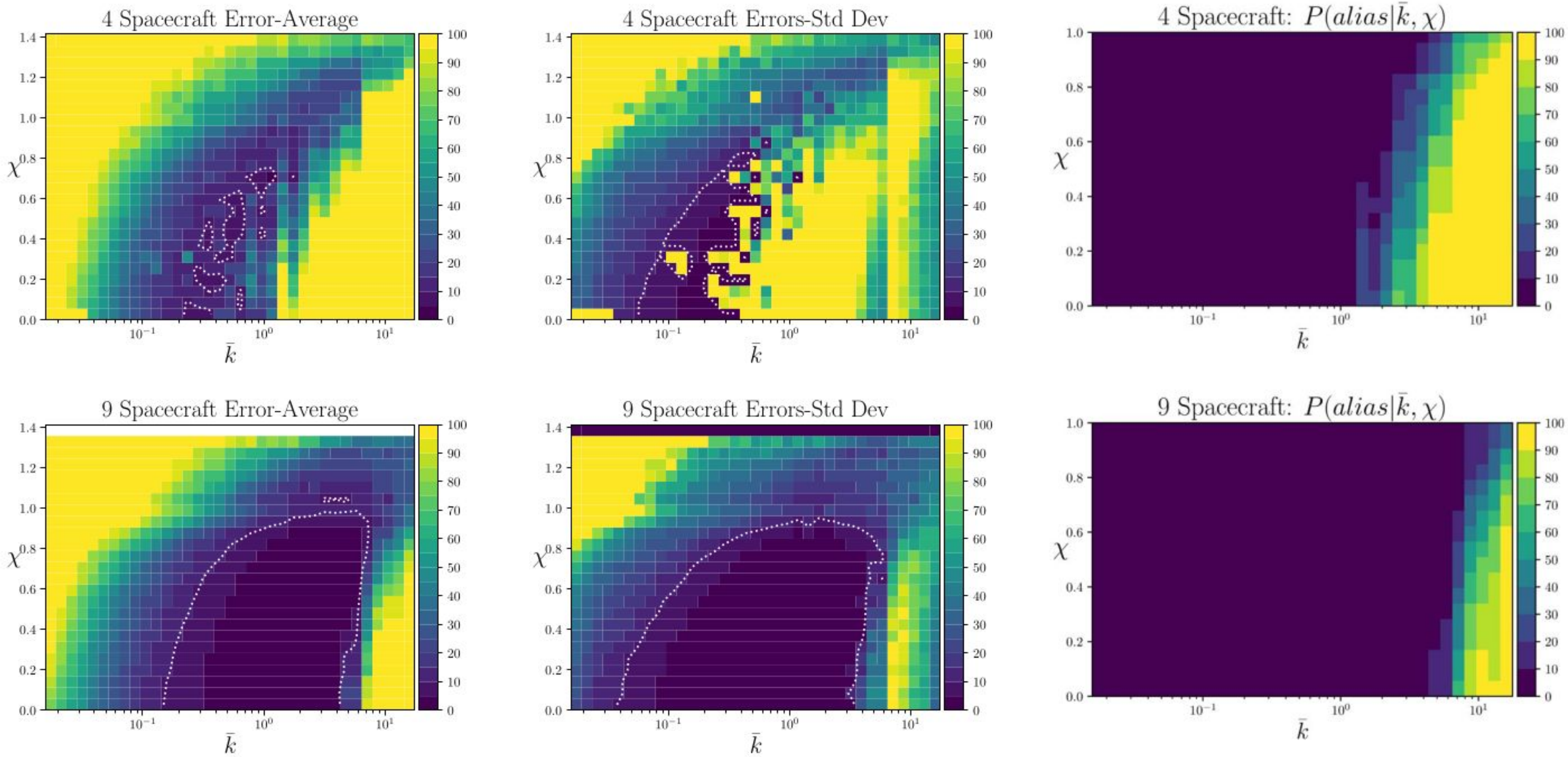

Modeled Error and Aliasing

Demonstrating that the error is log-normally distributed, we define a set of model equations for the error, uncertainty, and aliasing:

$$\sigma(\bar{k}, \chi) = c_0 + c_1 \log_{10} \bar{k} + c_2 \chi^2.$$

$$\mu(\bar{k}, \chi) = \log_{10}(a_0^{\chi - a_1} + a_2) + (a_3^{\chi - a_4} + a_5) \log_{10} \bar{k},$$

$$P(\text{alias}|\bar{k}, \chi) = \frac{1}{2}(1 + \tanh[4 \log_{10} \bar{k} + b_0 \chi^2 + b_1 \chi + b_2])$$

$$\mu_{\text{eff}}(\bar{k}, \chi) = [1 - P(\text{alias}|\bar{k}, \chi)]\, \mu(\bar{k}, \chi) + P(\text{alias}|\bar{k}, \chi) \max(400\bar{k}^{-1}, 100).$$

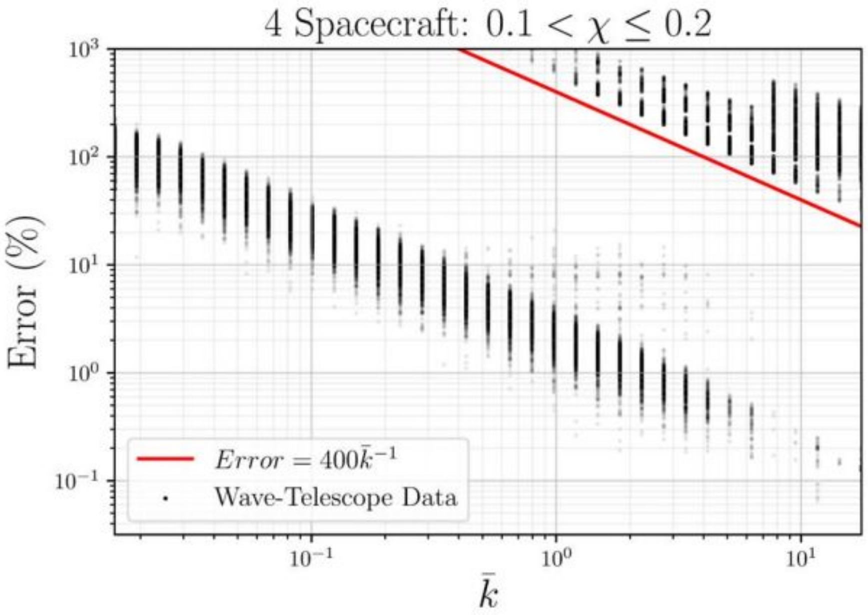

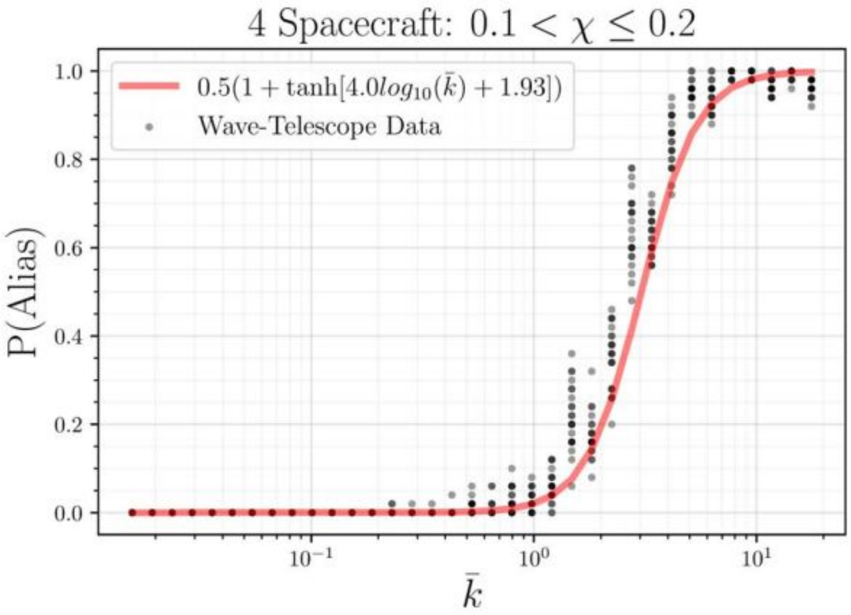

Posterior Predictive Check

We ‘learn’ the 12 coefficients via Bayesian inference, and verify that the learned equations and coefficients properly fit the data.

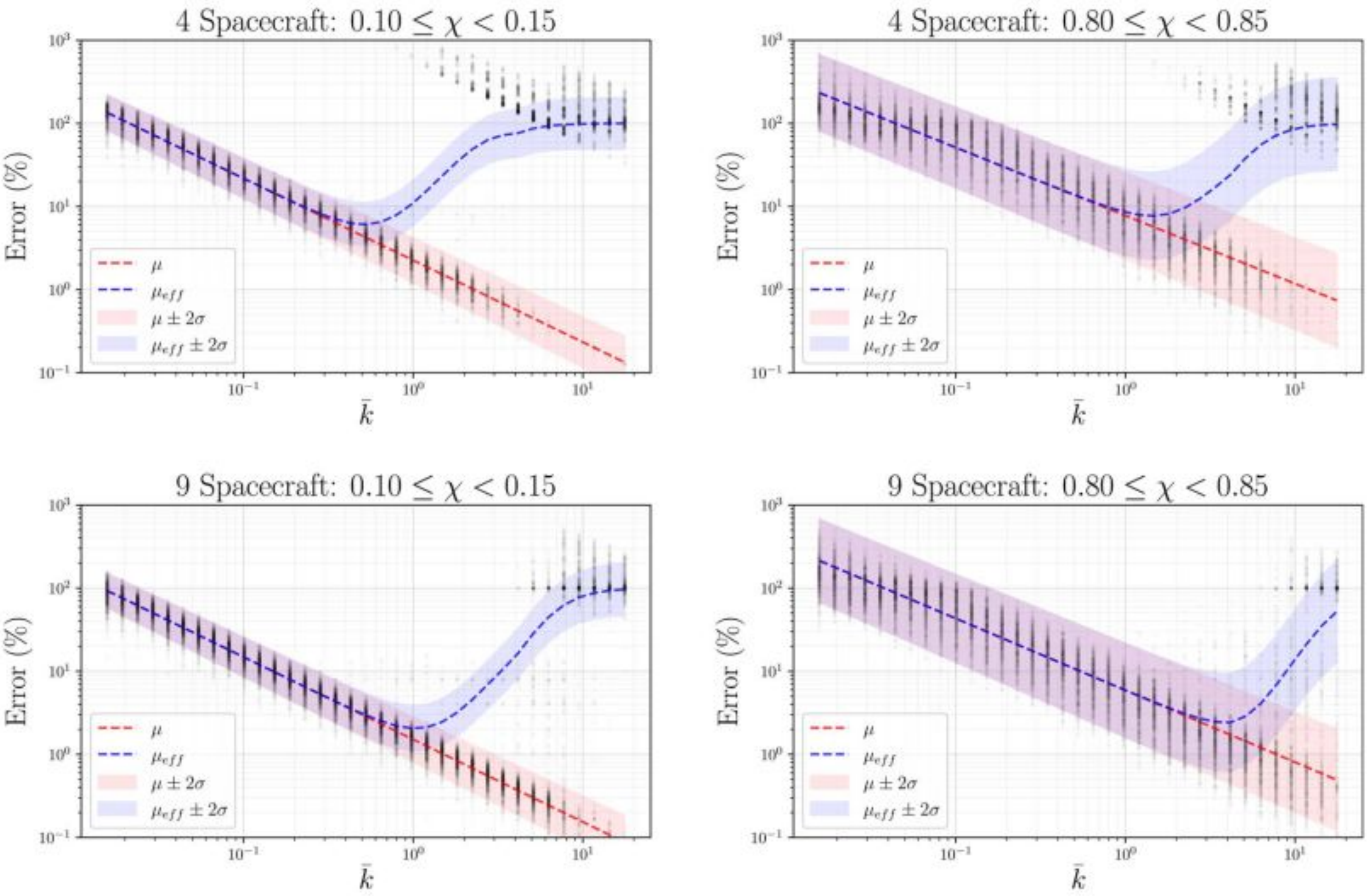

HelioSwarm Application of NEWTSS

With these equations, we introduce the Numerically Estimated Wave-Telescope Subset Selector, which determines the best polyhedra to resolve a wave at a given scale.

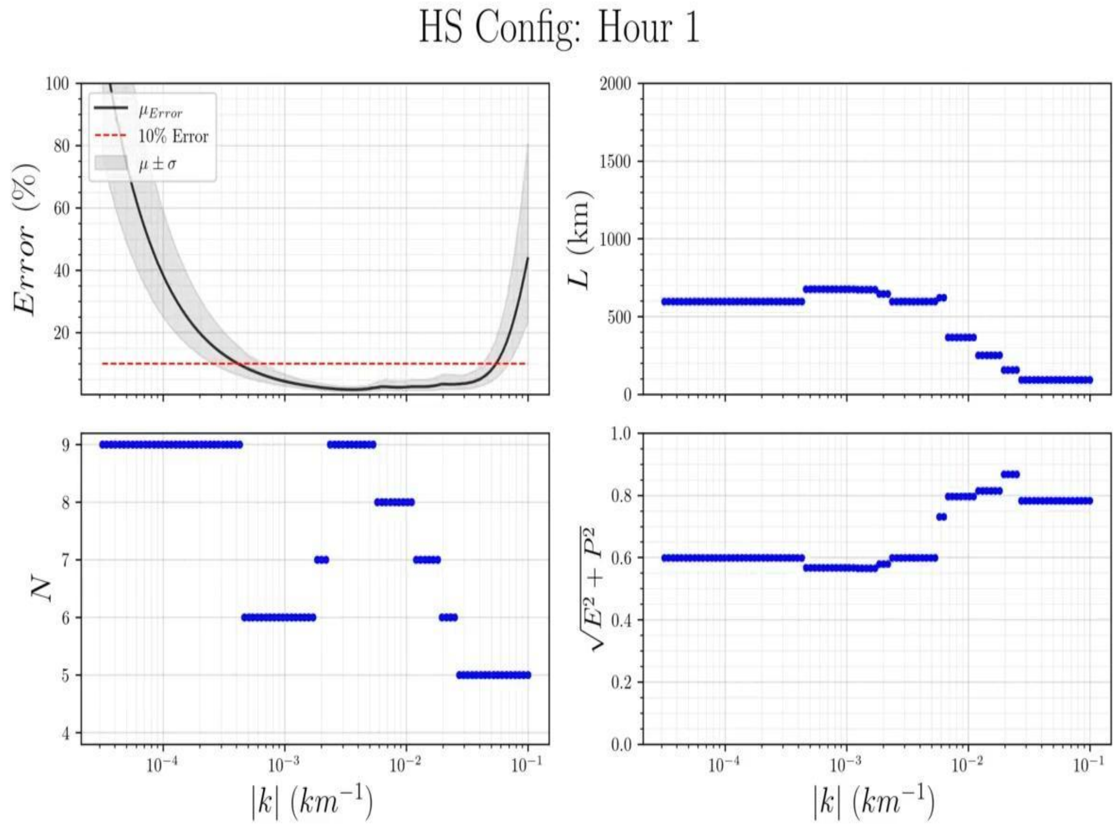

Method available
https://github.com/broeren/NEWTSS

See also example applications in Klein et al 2024 JGR

Field Reconstruction

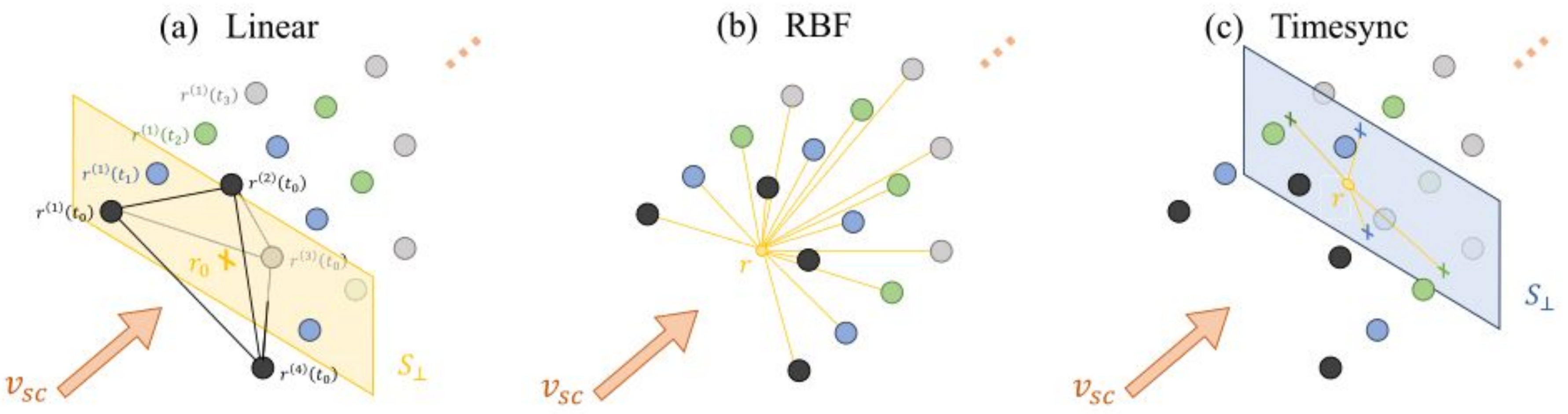

Instead of reconstructing the spectral power, let’s estimate a vector field at an unmeasured position.

FOTE (First Order Taylor Estimator)

Linear gradients can be used to locate specific features of magnetic field topology, including the existence and characteristics of nulls associated with magnetic reconnection.

Representing the magnetic field as

$$\mathbf{B}(\mathbf{r}) = \delta\mathbf{B} \cdot \mathbf{r}$$

Using the gradient tensor:

$$\delta B_{ij} = \partial B_i / \partial r_j$$

One can determine the distance **r** to the null. The eigenvalues of the gradient tensor can be used to classify the topology of the nulls:

$$\lambda_1 + \lambda_2 + \lambda_3 = \nabla \cdot \mathbf{B} = 0$$

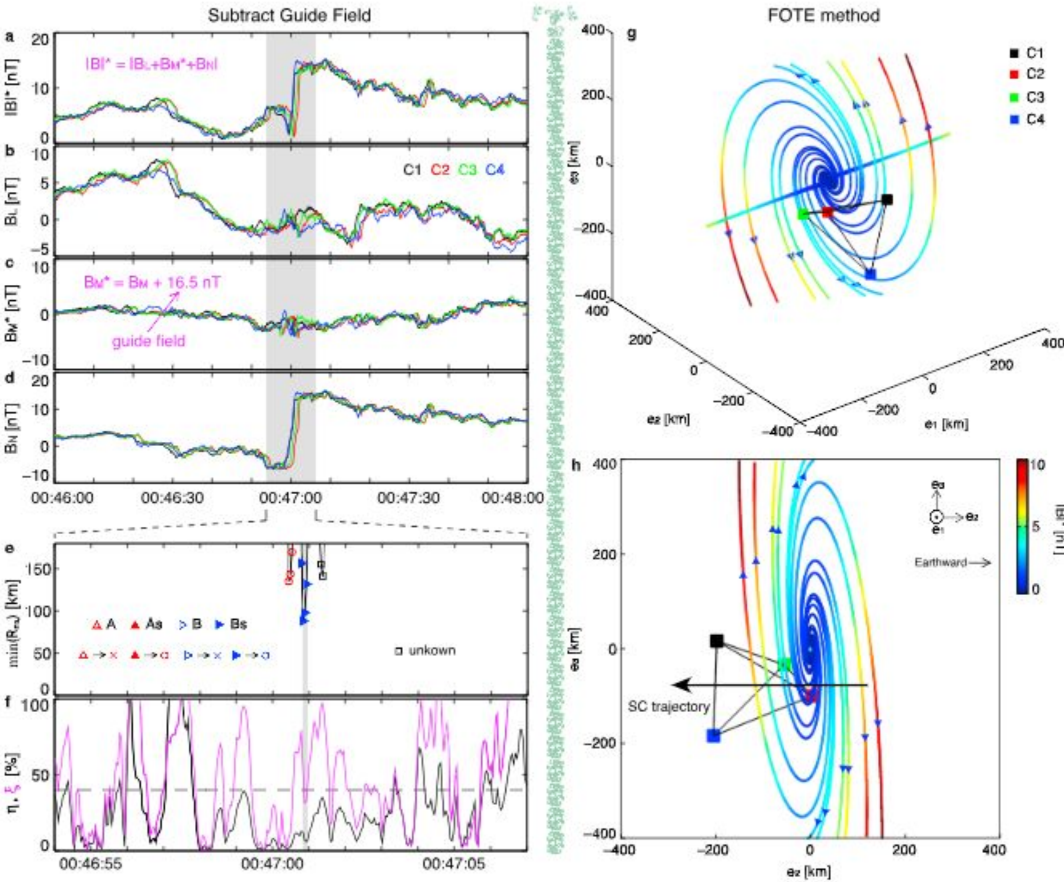

Fu et al 2015, 2016

Grad-Shafranov

z is the direction with *slow* variation compared to x,y

IF a system is representable by a 2D MHD equilibrium, we can solve for the partial vector potential A(x,y) by

$$\frac{\partial^2 A}{\partial x^2} + \frac{\partial^2 A}{\partial y^2} = -\mu_0 \frac{dP_t(A)}{dA} \qquad P_t = p + \frac{B_z^2}{2\mu_0}$$

1) MVA to identify variance direction
2) dHT frame transformation to verify equilibrium
3) Construction of GS plane
4) Transformation of temporal measurements to spatial profile
5) Integrate By(x,0) to obtain A(x,0) [Initial Value Solution]
6) Repeat Across GS Plane
7) Obtain Bx from 1st Order Taylor Expansion

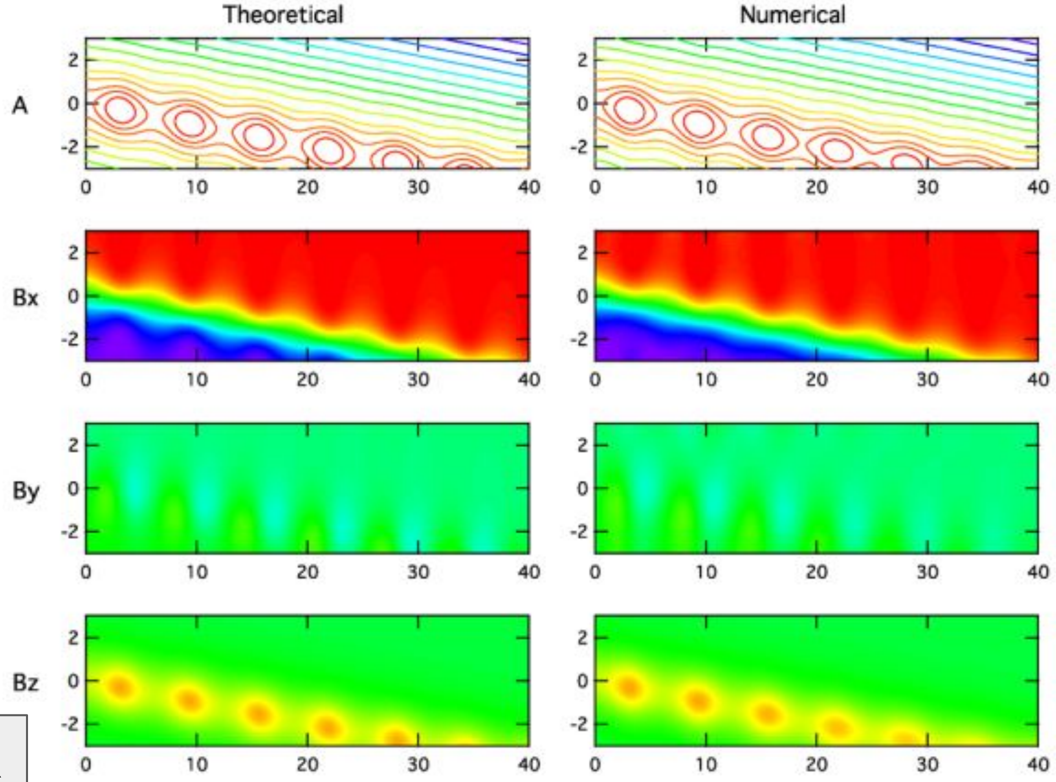

Hao and Sonnerup 1999, Sonnerup et al 2006

Multiple repos, e.g. https://github.com/PyGSDR

Grad-Shafranov Implementation

IF a system is representable by a 2D MHD equilibrium, this method works well.

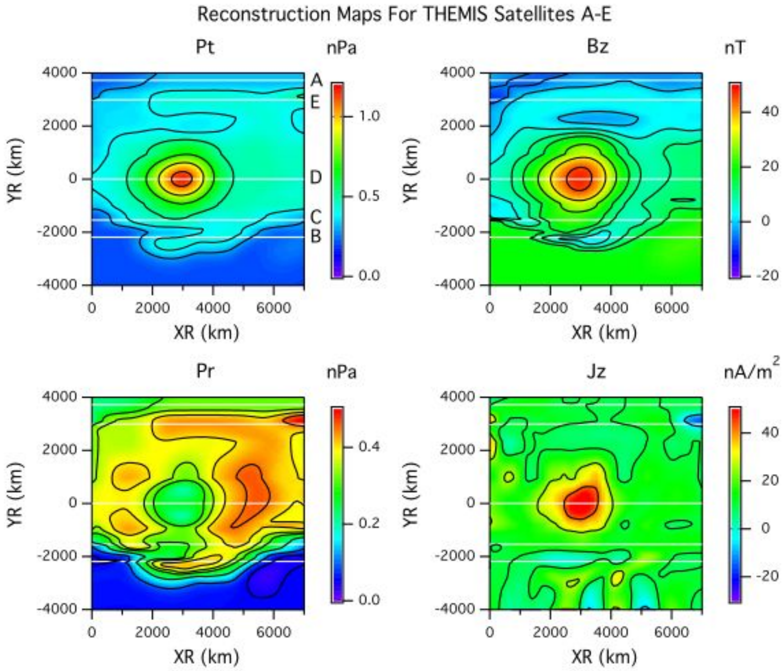

Lui et al 2008

Hu et al 2015

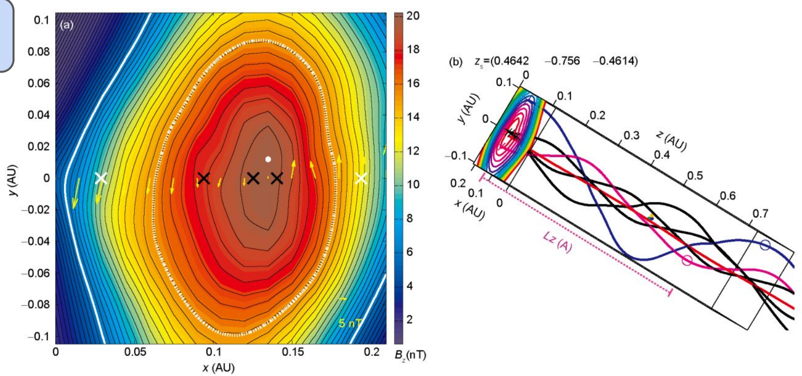

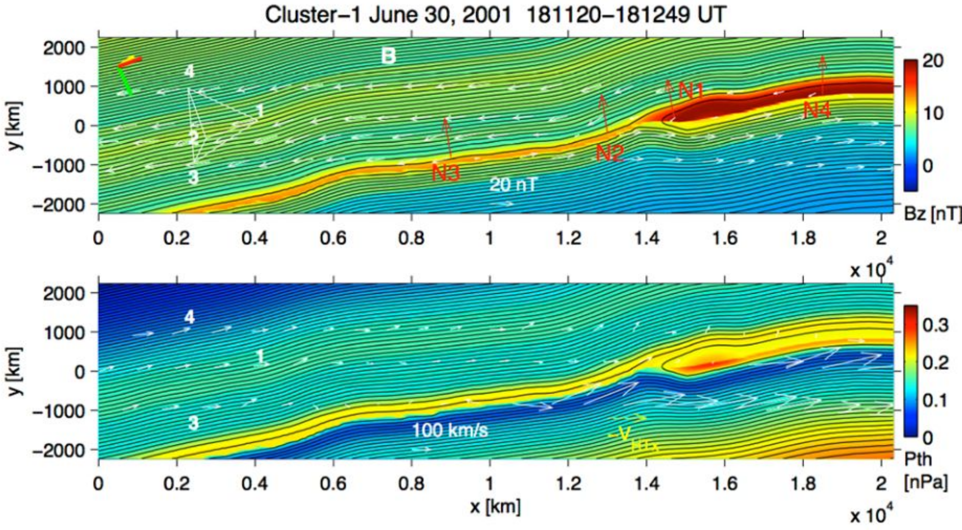

Hasegawa et al 2008

Hu 2017

Table 3 A table summarizing the GS and GS-type reconstructions[a)]

Structures recoverable	Assumption (s)	Input data	Field-line or streamline invariants	Applicable structures	Reference
2D magneto-hydrostatic structures	Magneto-hydrostatic	$\boldsymbol{B}$, plasma moments $(\boldsymbol{v}, p)^*$	$B_z(A)$, $p(A)$, $P_t(A)$	Current sheets of TD-type; fossil magnetic flux ropes	Hau and Sonnerup (1999); Hu and Sonnerup (2002, 2003)
2D structures with field-aligned flow	Steady, field-aligned, isentropic, MHD flow	$\boldsymbol{B}$, plasma moments $(\rho, \boldsymbol{v}, p)$	$S(A)$, $H(A)$, $G(A)$, $C_z(A)$	Current sheets of RD-type; flux ropes with field-aligned flow	Sonnerup et al. (2006); Teh et al. (2007)
2D structures with flow transverse to the magnetic field	Steady, isentropic, MHD flow; the magnetic field is along the invariant axis (z)	$\boldsymbol{B}$, plasma moments $(\rho, \boldsymbol{v}, p)$	S(ψ), $\widetilde{H}$ (ψ), F(ψ)	Flow vortices, e.g., of Kelvin-Helmholtz type	Sonnerup et al. (2006); Hasegawa et al. (2007a, 2009); Eriksson et al. (2009)
Ideal or resistive 2D MHD structures	Steady, MHD, isentropic (in the ideal case)	$\boldsymbol{B}$, plasma moments $(\rho, \boldsymbol{v}, p)$, $\boldsymbol{E}$ in the resistive case	$S(\psi)$ in the ideal case	Current sheets of TD- and RD-type; magnetic flux ropes	Sonnerup and Teh (2008); Teh and Sonnerup (2008); Eriksson et al. (2009)
Ideal or resistive 2D Hall-MHD structures	Steady, Hall-MHD, isentropic (in the ideal case)	$\boldsymbol{B}$, $\boldsymbol{E}$, ion moments $(\rho, \boldsymbol{v}, p)$	$S_i(\psi)$ & $S_e(\psi)$ in the ideal case	Current sheets of ion scale; ion diffusion regions of reconnection	Sonnerup and Teh (2009); Teh et al. (2011b)
Slowly evolving 2D magneto-hydrostatic structures	Magneto-hydrostatic, incompressible, frozen-in-flux	$\boldsymbol{B}$, plasma moments $(\boldsymbol{v}, p)$	$B_z(A)$, $p(A)$, $P_t(A)$, ρ(A)	Current sheets of TD-type; slowly evolving flux ropes	Sonnerup and Hasegawa (2010); Hasegawa et al. (2010)
3D magneto-hydrostatic structures	Magneto-hydrostatic	$\boldsymbol{B}$, plasma moments $(\boldsymbol{v}, p)$	p=*const.* Along field lines	Current sheets of TD-type; fossil magnetic flux ropes	Sonnerup and Hasegawa (2011)

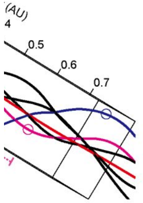

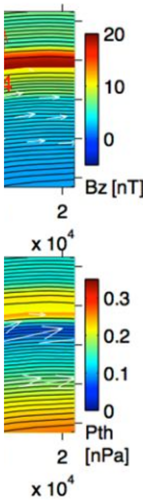

One shortcoming, or limitation of the GS reconstruction is that it is not guaranteed to work for every single case.
The set of metrics listed in Table 1 has to be assessed to judge whether the reconstruction result is acceptable.

Linear Field Reconstruction

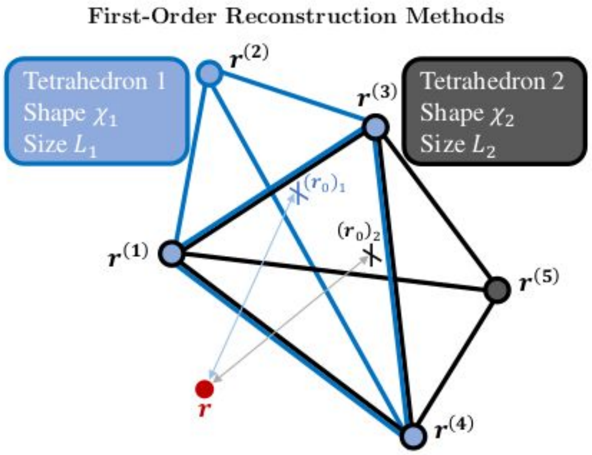

We use a Taylor Expansion to estimate the magnetic field using gradients from tetrahedral configurations, free from assuming an MHD equilibrium

$$\hat{B}_m^i = B_m + \sum_{k \in \{x,y,z\}} \partial_k B_m r_k^i \forall i \in \{1,2,3,4\}, m \in \{x,y,z\}.$$

We either average over all 128 tetrahedra, or a subset of that satisfy:

$$\| (r_0)_j - \xi \|_2 < L_j, \qquad \begin{matrix} \chi_j \leq 1 \\ \| (r_0)_j - \xi \|_2 < L_j. \end{matrix} \qquad \begin{matrix} \chi_j \leq 0.6 \\ \| (r_0)_j - \xi \|_2 < L_j. \end{matrix}$$

We also consider a second order estimation (Torbert et al 2022)

$$\hat{B}_m^i = B_m + \sum_{k \in \{x,y,z\}} \partial_k B_m r_k^i + \frac{1}{2} \sum_{j,k \in \{x,y,z\}} \partial_j \partial_k B_m r_k^i r_j^i \forall i \in \{1,\ldots,9\}, m \in \{x,y,z\}.$$

Broeren et al 2021 Frontiers

Sophisticated Selection of Gradients Improves Pointwise Error

$$\theta = 100\frac{\|\mathbf{B}_{calc}(\xi) - \mathbf{B}_{true}(\xi)\|_2}{\|\mathbf{B}_{true}(\xi)\|_2}$$

Overly restrictive methods reduce the reconstructed volume.

Application to Gkyell Turbulence Simulation

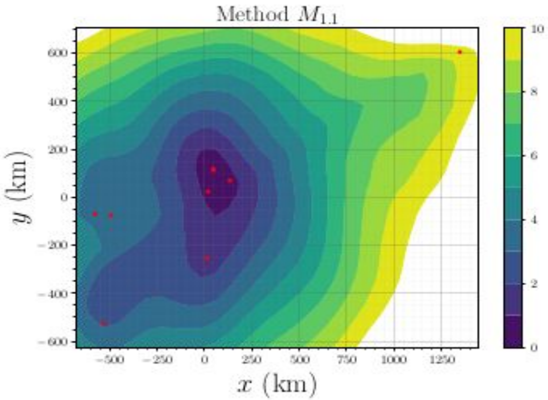

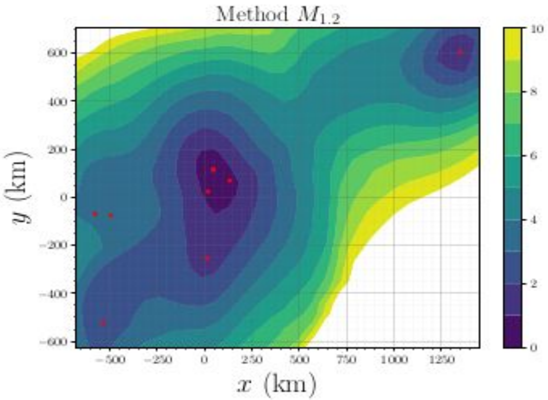

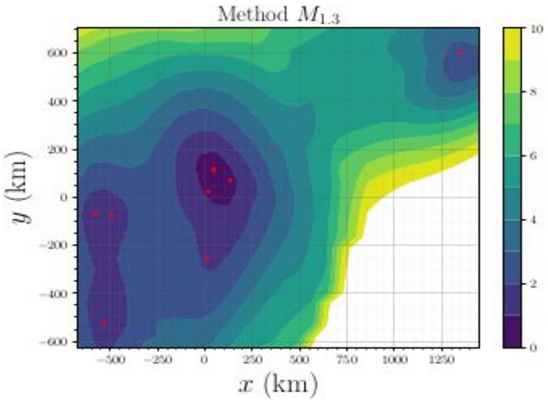

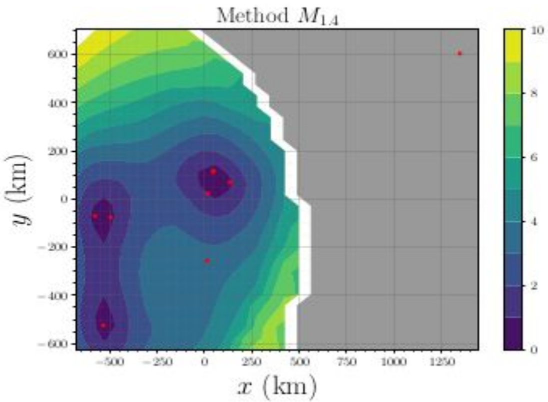

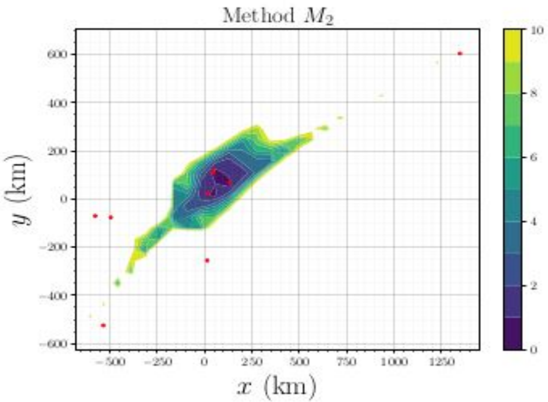

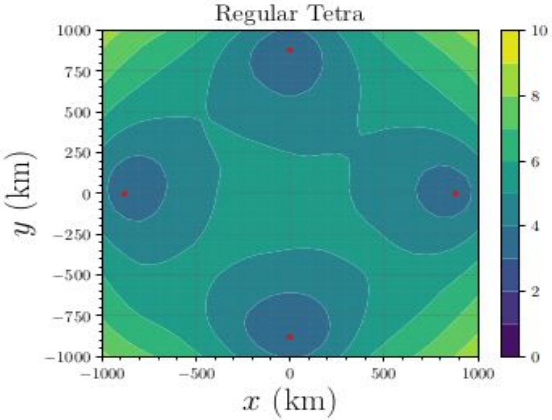

“The Physics Lives in the Derivatives”

$$\frac{\partial B_n}{\partial r_l} = \frac{1}{N^2}\left[\sum_{\alpha\neq\beta}\left(B_n^{(\alpha)} - B_n^{(\beta)}\right)\left(r_k^{(\alpha)} - r_k^{(\beta)}\right)\right]\overline{\overline{R}}_{kl}^{-1},$$

“Watanabe and Nagata, 2017 found that for a randomly generated set of sample points distributed in three-dimensions, the number of points included in the least-squares gradient computation greatly affects the accuracy of the local gradient estimation. This was determined by comparing the coarse grained velocity tensor (serving as the baseline true local gradient) to the spatial gradient computed via least-squares regression… **We find that for well-shaped configurations that are of correct relative size, we can very accurately estimate the local spatial gradient using only four points.**”

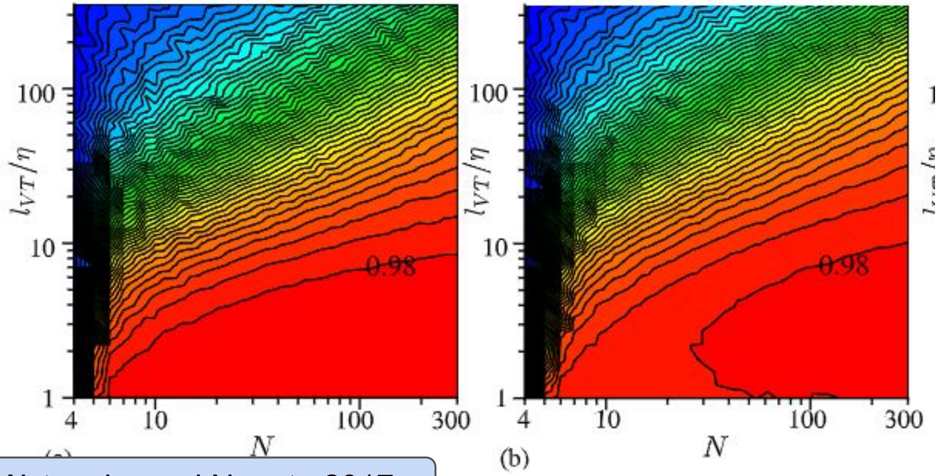

Watanabe and Nagata 2017

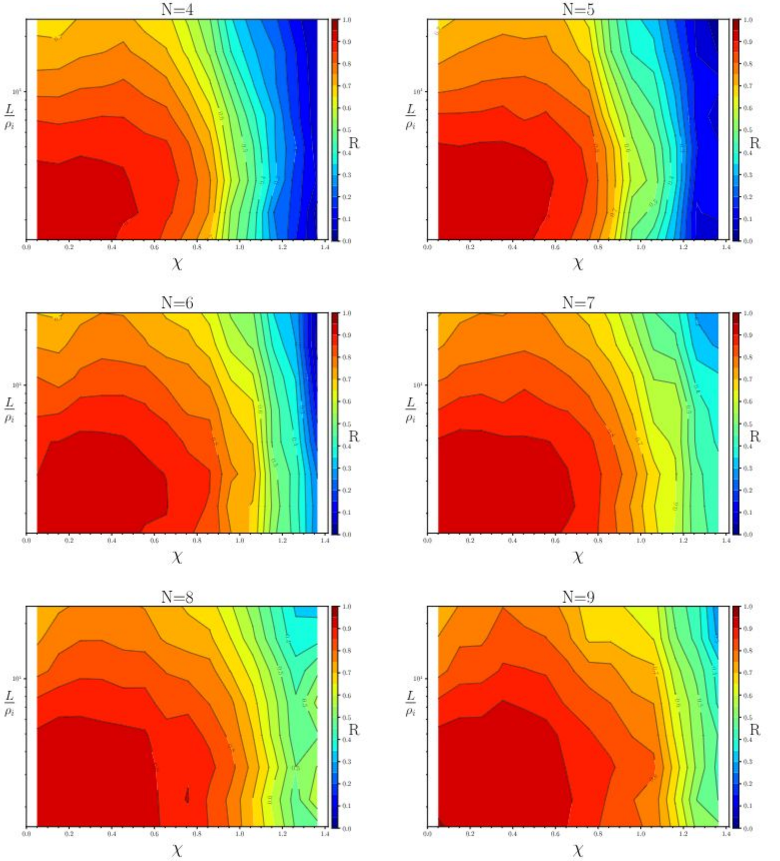

Broeren and Klein
https://arxiv.org/pdf/2405.14889

Radial Basis Functions

We estimate the magnetic field by a weighted average of the measured points, without the need of calculating gradients:

$$B_m(\mathbf{r}) = \sum_{i=1}^{N} \sum_{j=1}^{T} a_{i,j}\varphi(\|\mathbf{r}^{(i,j)} - \mathbf{r}\|) \qquad \forall\, m \in \{x, y, z\}.$$

$$\|\mathbf{x}\| := \sqrt{x_1^2 + x_2^2 + x_3^2}.$$

$$\varphi(\|\mathbf{r}^{(i,j)} - \mathbf{r}\|) = \sqrt{1 + (\|\mathbf{r}^{(i,j)} - \mathbf{r}\|/\sigma)^2}.$$

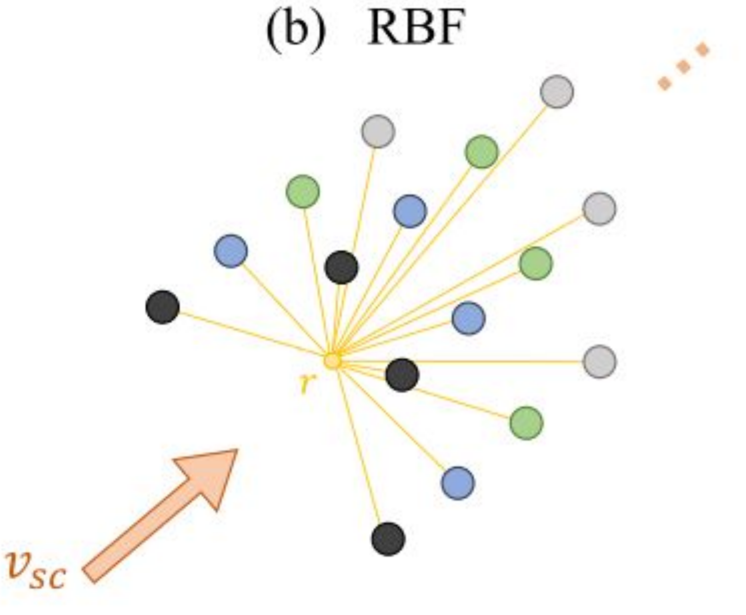

"While distance is counter-intuitively proportional to the multiquadric kernel function, the solution for the coefficient's a are inversely proportional to φ and proportional to the measured values of Bm(r (i,j)) (R. Hardy, 1990, Equation 9). This results in an interpolation scheme that weights nearby measured values most heavily, as desired. We refer the interested reader to theoretical math research of others for a detailed discussion pertaining to the validity of different kernel functions used in radial basis function approximation (Micchelli, 1984; Poggio & Girosi, 1990)."

Broeren et al 2024 EASS

Timesync

It is often the case that magnetic field measurements are taken with high temporal cadence, but with sparse spatial sampling. To reconstruct an arbitrary point, we treat the data in the V direction separately from the 2D perpendicular plane S⊥.

In the V direction, we use a 1D interpolation to produce each spacecraft's timeseries at an arbitrary time cadence.

At each point in time that we wish to reconstruct the magnetic field, we identify the plane that is perpendicular to vsc and also intersects the reconstructed point, S⊥.

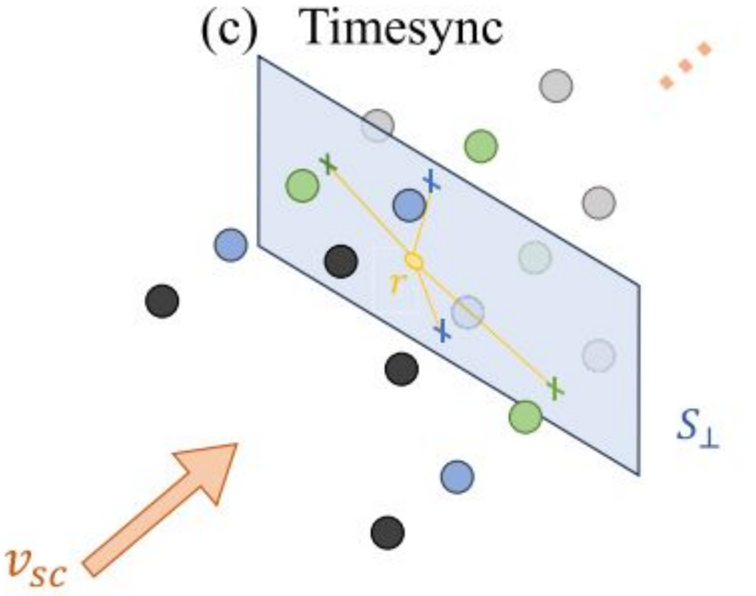

$$\mathbf{B}(\mathbf{r}) = \begin{cases} \dfrac{\sum_{i=1}^{N} w_i(\mathbf{r})\mathbf{B}(\mathbf{r}^{(i)})}{\sum_{i=1}^{N} w_i(\mathbf{r})} & \text{if } ||\mathbf{r}^{(i)} - \mathbf{r}|| \neq 0 \\ \mathbf{B}(\mathbf{r}^{(i)}) & \text{if } ||\mathbf{r}^{(i)} - \mathbf{r}|| = 0 \end{cases}$$

$$w_i = \frac{1}{||\mathbf{r}^{(i)} - \mathbf{r}||^2}.$$

Broeren et al 2024 EASS

We perform a 2D inverse distance weighted interpolation on each S⊥ plane independently to estimate values spanning this surface. **There is only one measurement per spacecraft that is taken into account for these 2D reconstructions:** each 1D-interpolated measurement from the spacecraft's timeseries gives one value on S⊥

A Comparison between Linear, RBF, Timesync

We can compare the pointwise accuracy of these different reconstruction methods, focusing on the volume where the methods have a fair chance of capturing.

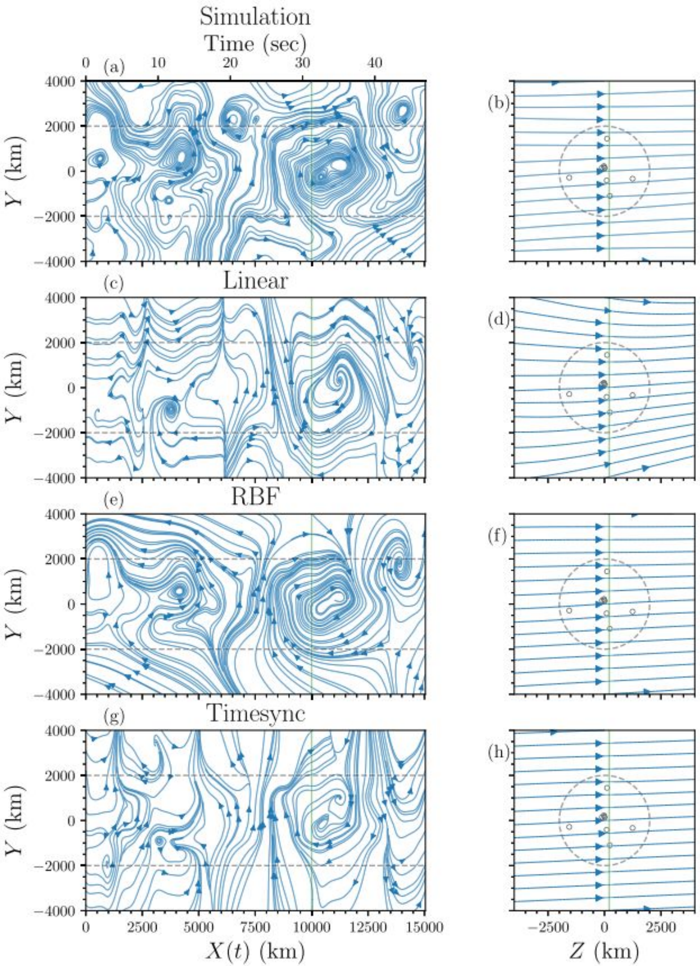

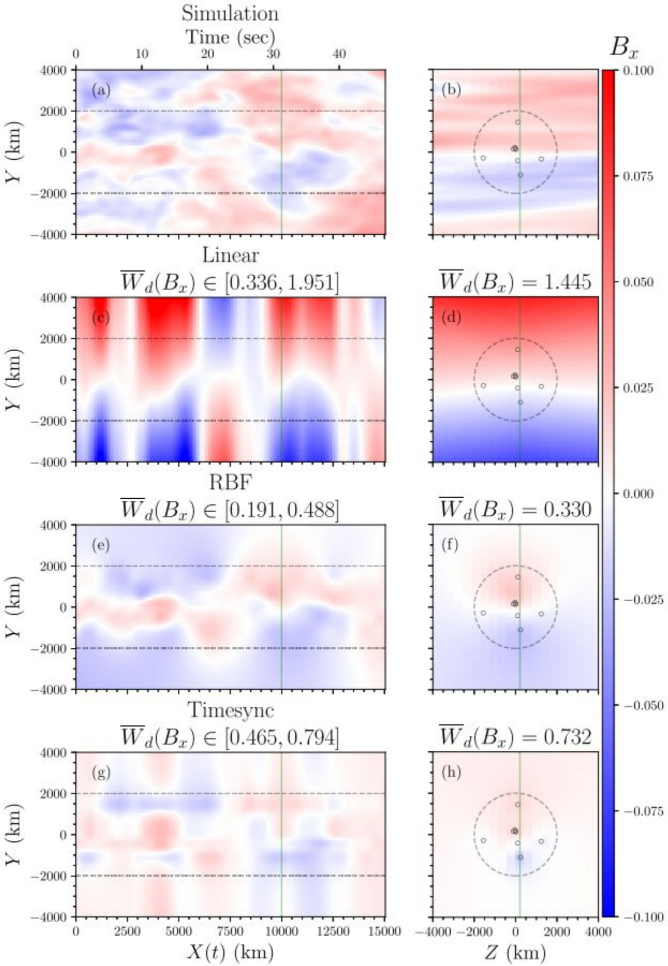

Broeren et al 2024 EASS

Error Evaluation: Point Wise Error

$$\text{Error} = 100\,\frac{\|\mathbf{B}_{recon} - \mathbf{B}_{sim}\|}{\|\mathbf{B}_{sim}\|},$$

RBF and Timesync yield larger volumes of lower pointwise error.

Table 1

Fraction of Region Within a Distance of 2L (Where L = 2,000 km) From the Three Spacecraft Barycenters That Are Reconstructed With an Error of Less Than 20%, 15%, 10%, 5%, and 1% for Each of the Spacecraft Configurations and Three Reconstruction Methods

Method	Error threshold	Config A	Config B	Config C
Linear	20%	0.954	0.981	0.674
	15%	0.688	0.805	0.502
	10%	0.285	0.428	0.311
	5%	0.002	0.021	0.064
	1%	0.000	0.000	0.000
RBF	20%	1.000	1.000	1.000
	15%	0.982	0.997	0.994
	10%	0.643	0.742	0.711
	5%	0.139	0.247	0.196
	1%	0.004	0.012	0.013
Timesync	20%	1.000	1.000	1.000
	15%	0.986	0.990	0.966
	10%	0.668	0.683	0.571
	5%	0.192	0.249	0.170
	1%	0.006	0.009	0.006

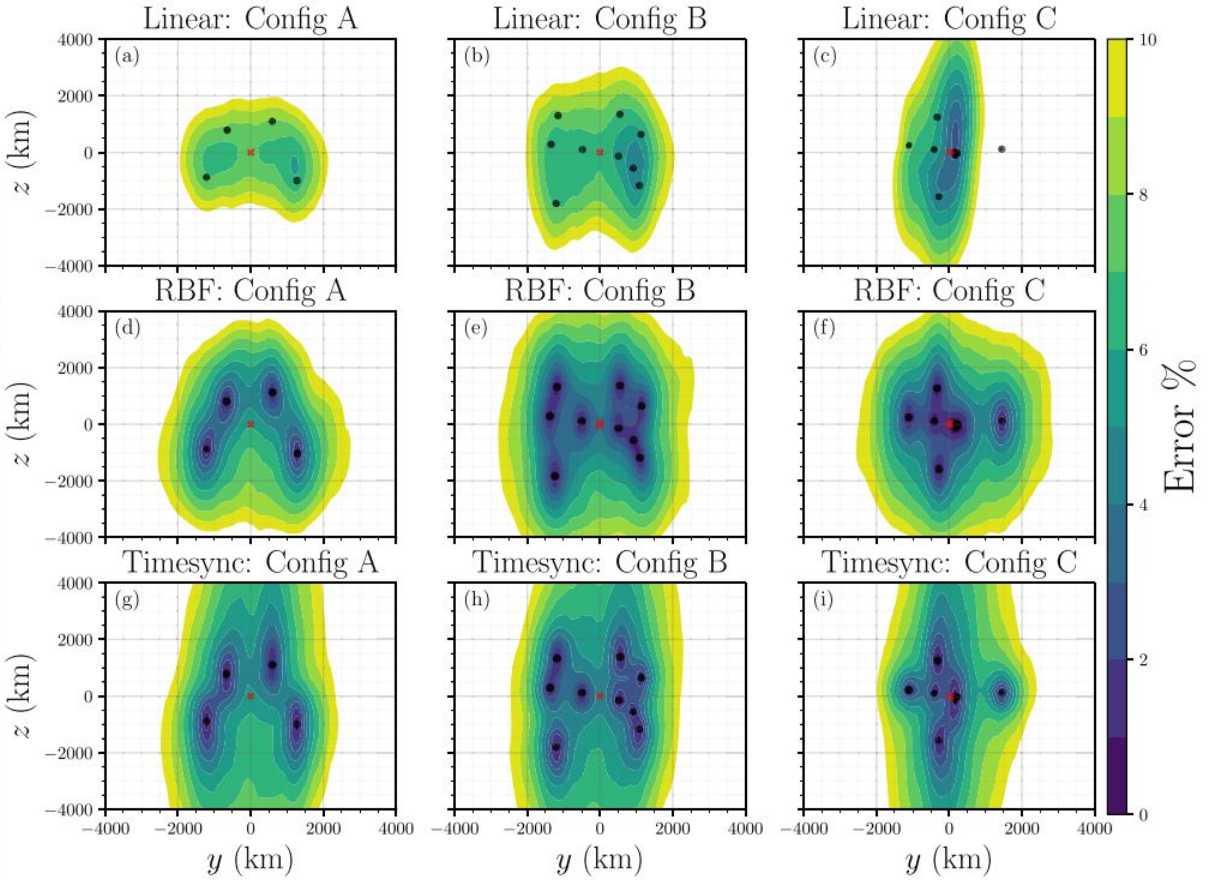

Error Evaluation: Wasserstein Distance

Absolute error will not always be the ideal error metric, especially for turbulent fields with intermittent structures.

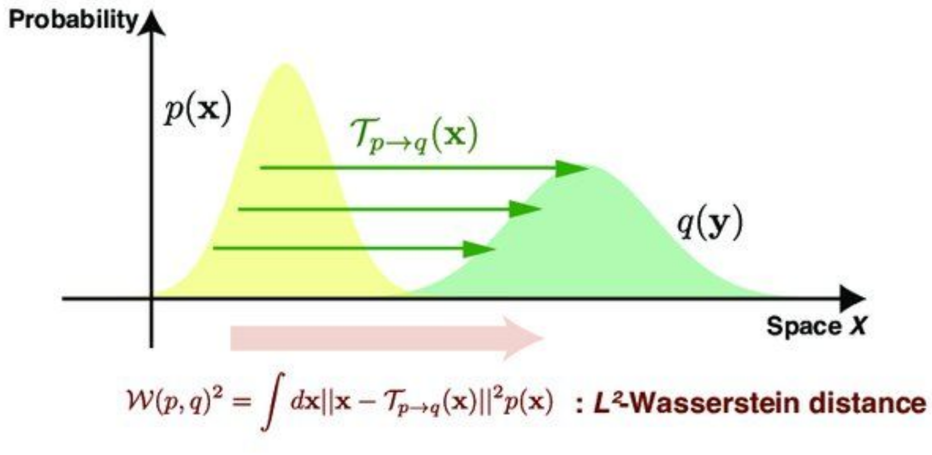

Nakazato et al 2021

$$W_d(f,g) = \inf_{\pi} \left(\frac{1}{n} \sum_{i=1}^{n} \|f_i - g_{\pi(i)}\|^p \right)^{1/p},$$

"Visualize one of the distributions we wish to compare as piles of earth, and the other as a collection of holes in the earth. In this visualization, the Earth movers distance measures the least amount of work needed to fill the holes with earth, if a unit of work corresponds to transporting a unit of earth by a unit of ground distance."

-Rubner and Tomasi (2001)

Is the Reconstructed Field Better than a Constant Value?

We define a variation of this error metric, *the relative Wasserstein distance*, to compare the topological similarity of two magnetic fields.

$$\overline{W}_d(B_{recon}, B_{sim}) = \frac{W_d(B_{recon}, B_{sim})}{W_d\left(\tilde{B}_{sim}, B_{sim}\right)}.$$

Again, the linear method is uniformly worse than the other two methods, frequently being about as accurate as just describing the field with a constant value.

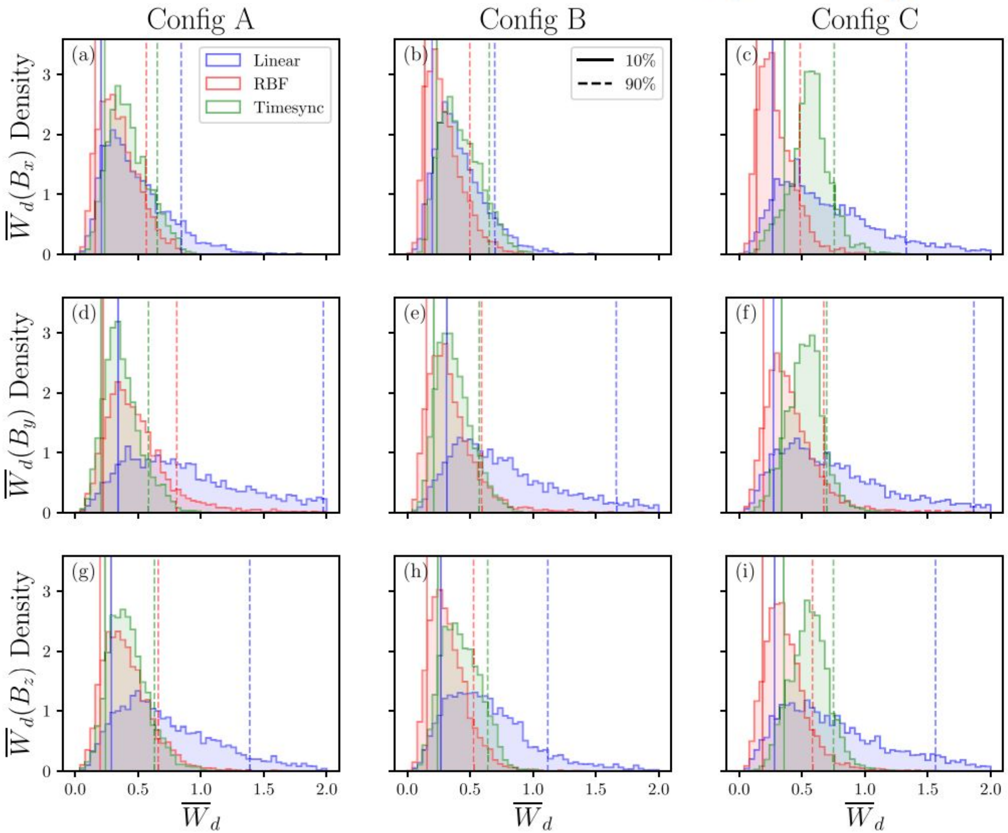

Table 2
Median Relative Wasserstein Distances (Equation 12) for Each Spacecraft Configuration (Columns A, B, C) and Magnetic Field Reconstruction Method as a Function of Each Magnetic Field Component B_x, B_y, B_z (Rows)

Method	Component	Config A	Config B	Config C
Linear	B_x	0.421	0.382	0.614
	B_y	0.847	0.709	0.702
	B_z	0.664	0.590	0.694
RBF	B_x	0.322	0.263	0.266
	B_y	0.437	0.308	0.372
	B_z	0.381	0.300	0.342
Timesync	B_x	0.403	0.405	0.565
	B_y	0.354	0.355	0.527
	B_z	0.403	0.415	0.557

Future Methods: Physics Informed Neural Networks

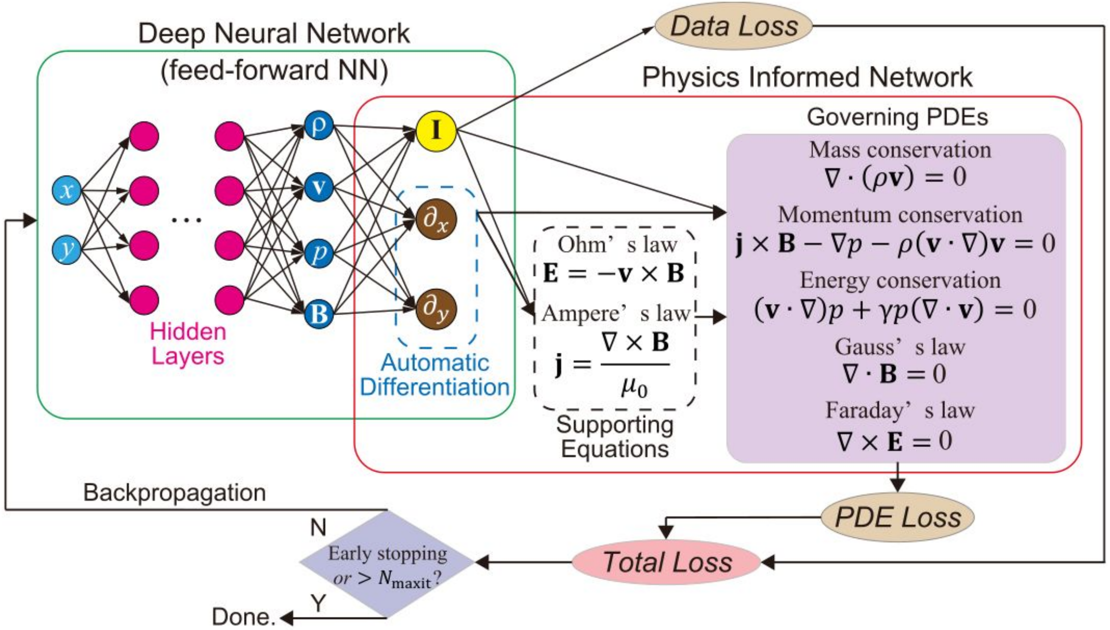

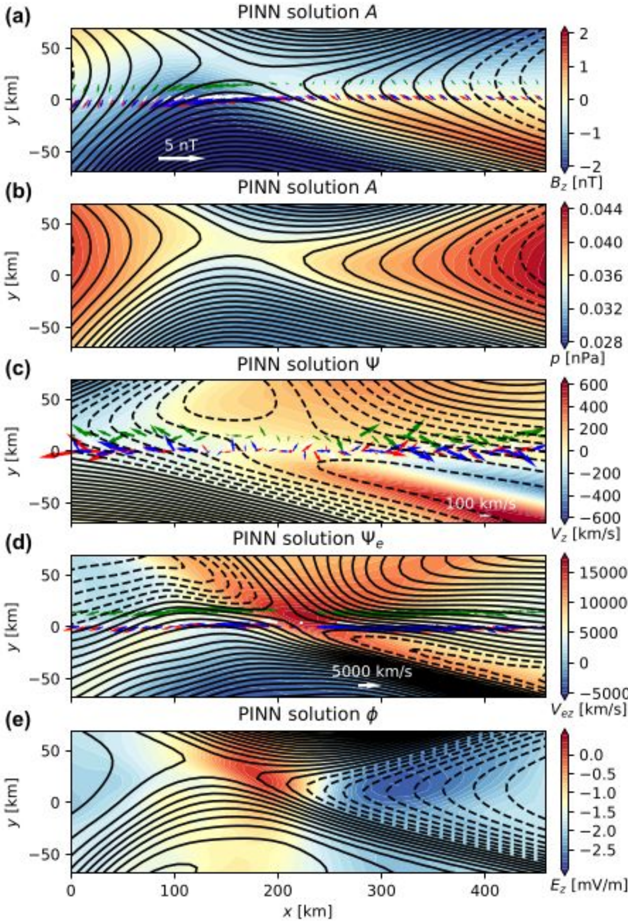

"Our results demonstrate that the PINN-based method provides a flexible and powerful new tool for revealing plasma structures around observing spacecraft, particularly in regions where **model assumptions may be only approximately valid.**"

Hasegawa et al 2026 JGR

Backup Slides

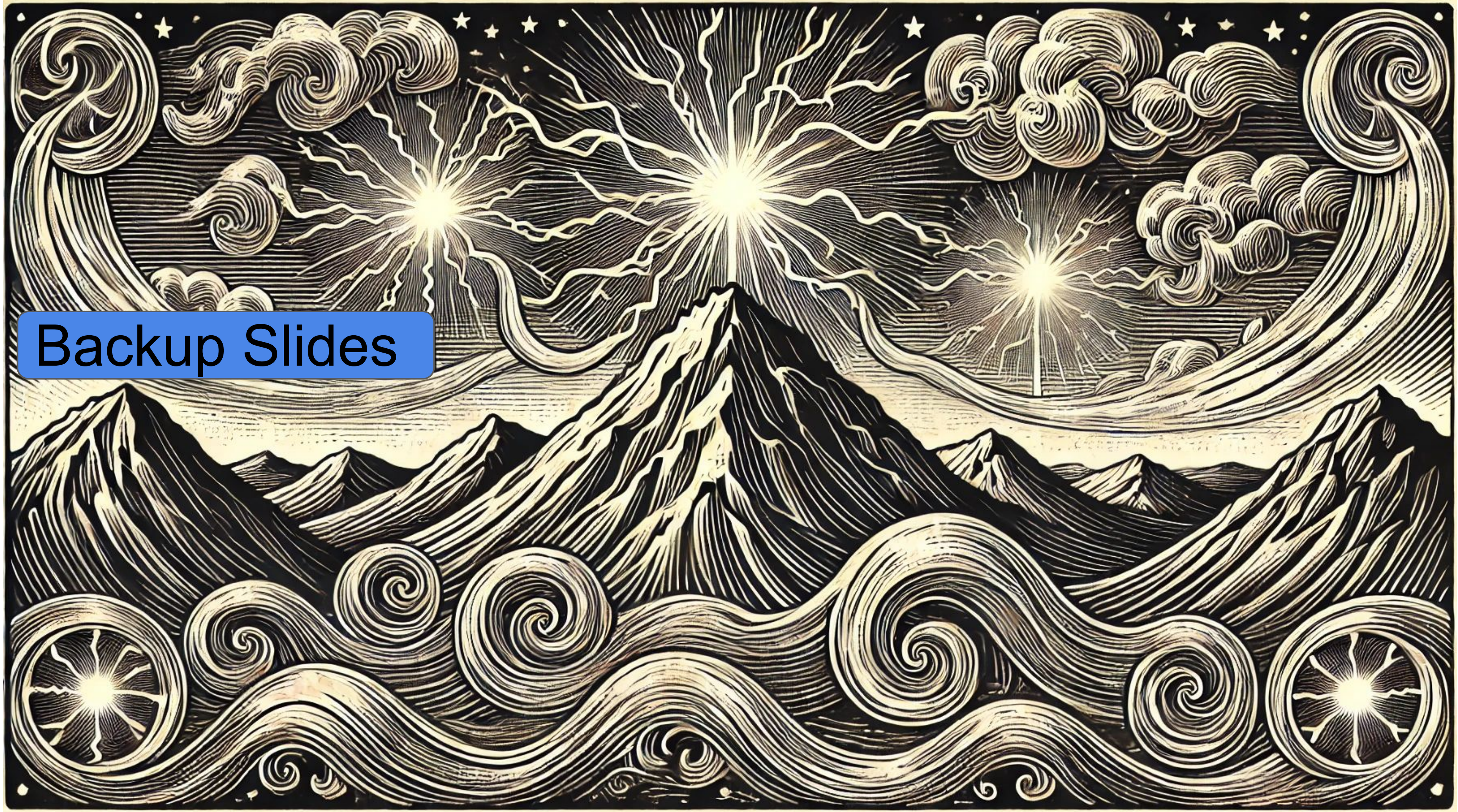

The Linear Plasma Response:

Stix 1993, Chapter 10

$$\mathbf{j} = \sum_s \mathbf{j}_s = \sum_s q_s \int d^3\mathbf{v}\mathbf{v}_s \delta f_s(\mathbf{x},\mathbf{v},t) = -\frac{i\omega}{4\pi}\sum_s \underline{\underline{\chi}}_s \cdot \mathbf{E} \qquad \epsilon(\omega,\mathbf{k}) = \underline{\underline{1}} + \sum_s \underline{\underline{\chi}}_s(\omega,\mathbf{k})$$

Moving charged particles and electromagnetic fields can be coupled through susceptibility tensors □$_s$, enabling the calculation of the dielectric of the medium ε.

$$\underline{\underline{\chi}}_s = \frac{\omega_{p,s}^2}{\omega\Omega_{0,s}}\int_0^\infty 2\pi p_\perp dp_\perp \int_{-\infty}^{\infty} dp_\parallel$$

$$\left[\hat{e}_\parallel\hat{e}_\parallel \frac{\Omega_s}{\omega}\left(\frac{1}{p_\parallel}\frac{\partial f_{s,0}}{\partial p_\parallel} - \frac{1}{p_\perp}\frac{\partial f_{s,0}}{\partial p_\perp}\right)p_\parallel^2 + \sum_{n=-\infty}^{\infty}\frac{\Omega_s p_\perp U}{\omega - k_\parallel v_\parallel - n\Omega_s}\underline{\underline{T}}_n\right] \qquad \underline{\underline{T}}_n = \begin{pmatrix} \frac{n^2 J_n^2}{z^2} & \frac{inJ_nJ_n'}{z} & \frac{nJ_n^2 p_\parallel}{zp_\perp} \\ -\frac{inJ_nJ_n'}{z} & (J_n')^2 & \frac{-iJ_nJ_n'p_\parallel}{p_\perp} \\ \frac{nJ_n^2p_\parallel}{zp_\perp} & \frac{iJ_nJ_n'p_\parallel}{p_\perp} & \frac{J_n^2p_\parallel^2}{p_\perp^2} \end{pmatrix}.$$

$$U = \frac{\partial f_{0,s}}{\partial p_\perp} + \frac{k_\parallel}{\omega}\left(v_\perp \frac{\partial f_{0,s}}{\partial p_\parallel} - v_\parallel \frac{\partial f_{0,s}}{\partial p_\perp}\right)$$

Linearize Faraday's and Ampere's laws, assume a plane wave solution of the form **exp (- i ωt + kx)**, we can combine these expressions to form the familiar wave equation

$$\underline{\underline{\Lambda}}\cdot\mathbf{E} = \begin{pmatrix} \epsilon_{xx} - n_z^2 & \epsilon_{xy} & \epsilon_{xz} + n_xn_z \\ \epsilon_{yx} & \epsilon_{yy} - n_x^2 - n_z^2 & \epsilon_{yz} \\ \epsilon_{zx} + n_xn_z & \epsilon_{zy} & \epsilon_{zz} - n_x^2 \end{pmatrix}\begin{pmatrix} E_x \\ E_y \\ E_z \end{pmatrix} = 0.$$

Bi-Maxwellian Plasma Waves:

Stix 1993, Chapter 10

The main difficulty to solving for □$_s$ are integrals of the form:
which for an arbitrary f do not have a closed solution.

$$\int dp_\perp \int dp_\parallel p_\perp^n p_\parallel^m \frac{\partial f_s}{\partial \mathbf{p}}$$

A typical solution is to impose a form for f that does have a closed solution, e.g. a bi-Maxwellian:

$$f_{0j} = \frac{1}{\pi^{3/2} m_j^3 w_{\perp j}^2 w_\parallel} \exp\left(-\frac{p_\perp^2}{m_j^2 w_{\perp j}^2} - \frac{(p_\parallel - m_j U_j)^2}{m_j^2 w_{\parallel j}^2} \right),$$

Solutions for the underlying integral can be expressed in terms of Bessel Functions and the Plasma Dispersion Function Z_0 (Fried & Conte), yielding:

$$\chi_s = \left[\hat{\mathbf{e}}_\parallel \hat{\mathbf{e}}_\parallel \frac{2\omega_p^2}{\omega k_\parallel w_\perp^2} \langle v_\parallel \rangle + \frac{\omega_p^2}{\omega} \sum_{n=-\infty}^{\infty} e^{-\lambda} \mathbf{Y}_n(\lambda) \right]_s, \tag{57}$$

$$\mathbf{Y}_n(\lambda) =$$

$$\begin{pmatrix} \frac{n^2 I_n}{\lambda} A_n & -in(I_n - I_n')A_n & \frac{k_\perp}{\Omega} \frac{n I_n}{\lambda} B_n \\ in(I_n - I_n')A_n & \left(\frac{n^2}{\lambda} I_n + 2\lambda I_n - 2\lambda I_n' \right) A_n & \frac{ik_\perp}{\Omega}(I_n - I_n')B_n \\ \frac{k_\perp}{\Omega} \frac{n I_n}{\lambda} B_n & -\frac{ik_\perp}{\Omega}(I_n - I_n')B_n & \frac{2(\omega - n\Omega)}{k_\parallel w_\perp^2} I_n B_n \end{pmatrix}$$

$$A_n = \frac{1}{\omega} \frac{T_\perp - T_\parallel}{T_\parallel} + \frac{1}{k_\parallel w_\parallel} \frac{(\omega - k_\parallel V - n\Omega)T_\perp + n\Omega T_\parallel}{\omega T_\parallel} Z_0,$$

$$B_n = \frac{1}{k_\parallel} \frac{(\omega - n\Omega)T_\perp - (k_\parallel V - n\Omega)T_\parallel}{\omega T_\parallel}$$

$$+ \frac{1}{k_\parallel} \frac{\omega - n\Omega}{k_\parallel w_\parallel} \frac{(\omega - k_\parallel V - n\Omega)T_\perp + n\Omega T_\parallel}{\omega T_\parallel} Z_0,$$

$$Z_0 = Z_0(\zeta_n), \quad \zeta_n = \frac{\omega - k_\parallel V - n\Omega}{k_\parallel w_\parallel}, \tag{66}$$

$$\frac{dZ_0(\zeta_n)}{d\zeta_n} = -2[1 + \zeta_n Z_0(\zeta_n)].$$

This has been done numerically for decades, e.g. Gary 1993, or the WHAMP, NHDS, or PLUME Codes.

Plasma in a **L**inear **U**niform **M**agnetized **E**nvironment

Klein & Howes 2015 PoP
Klein, Howes, Brown 2025 RNAAS

PLUME is available at https://github.com/kgklein/PLUME

PLUME solves the bimaxwellian dispersion relation for arbitrary numbers of bi-Maxwellian components, yielding the frequency, eigenfunctions, and heating rates.

Tutorial on installing and using PLUME

Dimensionless Global Inputs			
Reference Parallel Plasma Beta	$\beta_{\parallel R} = 8\pi n_R T_{\parallel R}/B_0^2$	Reference Parallel Thermal Velocity	$\overline{w}_{\parallel R} = w_{\parallel R}/c$
Reference Perpendicular Wavenumber	$\overline{k}_\perp = k_\perp \rho_R$	Reference Parallel Wavenumber	$\overline{k}_\parallel = k_\parallel \rho_R$
Dimensionless Species Inputs			
Relative Parallel Temperature	$\tau_s = T_{\parallel R}/T_{\parallel s}$	Temperature Anisotropy	$\aleph_s = T_{\perp s}/T_{\parallel s}$
Mass Ratio	$\mu_s = m_R/m_s$	Charge Ratio	$Q_s = q_R/q_s$
Density Ratio	$D_s = n_s/n_R$	Drift Velocity	$\overline{V}_s = V_s/v_{AR}$
Outputs			
Real Frequency	$\overline{\omega}_R = \omega_r/\Omega_R$	Imag. Frequency	γ/Ω_R
Electric Eigenmode	$\mathbf{E}/E_x$	Magnetic Eigenmode	$\mathbf{B}/E_x$
Species Density Eigenmode	$n_{1,s}/(n_{0,s}E_x/B_0)$	Species Bulk Velocity Eigenmode	$\mathbf{U}_s/(cE_x/B_0)$
Power Absorp. Spec. Landau Damp.	$P_s^{LD} = \gamma_s^{LD}/\lvert\omega_r\rvert$	Power Absorp. Spec. Trans. Time Damp.	$P_s^{TTD} = \gamma_s^{TTD}/\lvert\omega_r\rvert$
Power Absorp. Spec. Cyclotron Damp.[a]	$P_s^{CD,n} = \gamma_s^{CD,n}/\lvert\omega_r\rvert$		

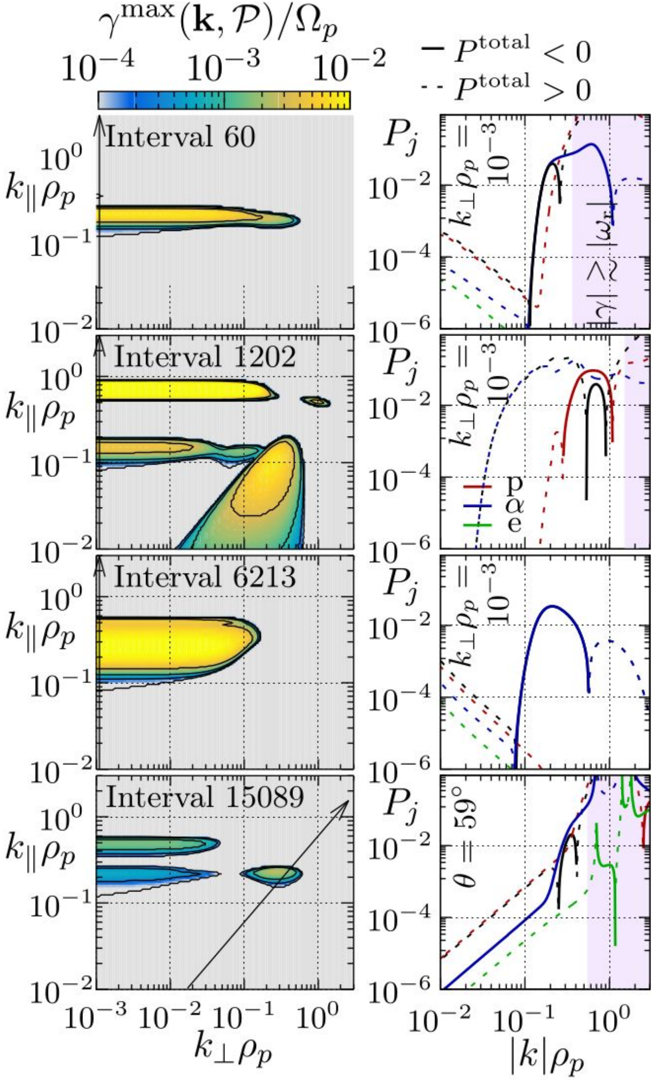

Aliasing

Spatial aliasing may produce misleading signals and unphysical interpretations.

Learned Coefficients

With our ensemble of waves and configurations, we learn the best values for these 12 coefficients for each N between 4 and 9 spacecraft.

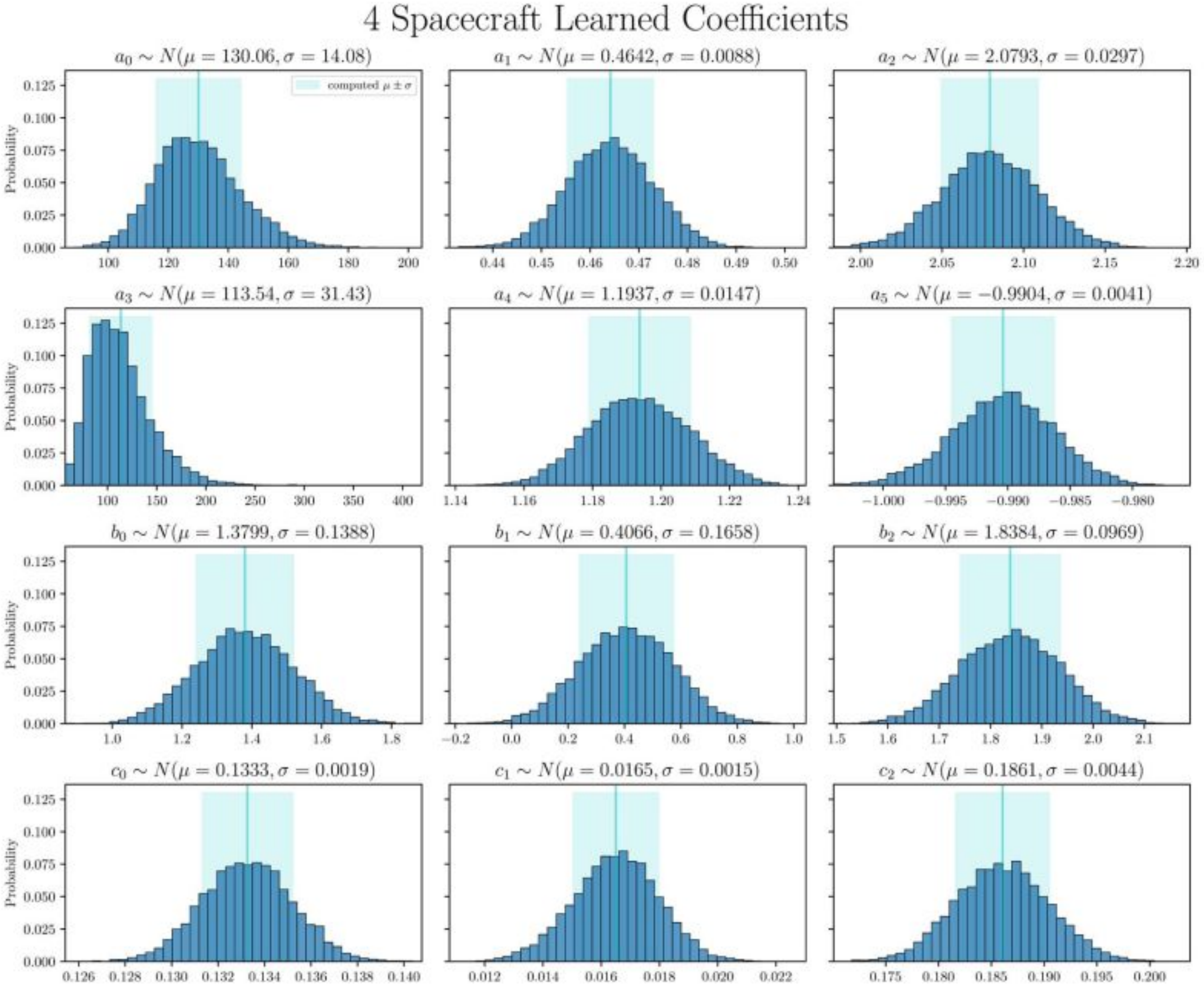

Wavevector Accuracy Span

Given these equations and coefficients, we can determine the range of wavevectors that can be accurately constructed for N spaces with a given geometry:

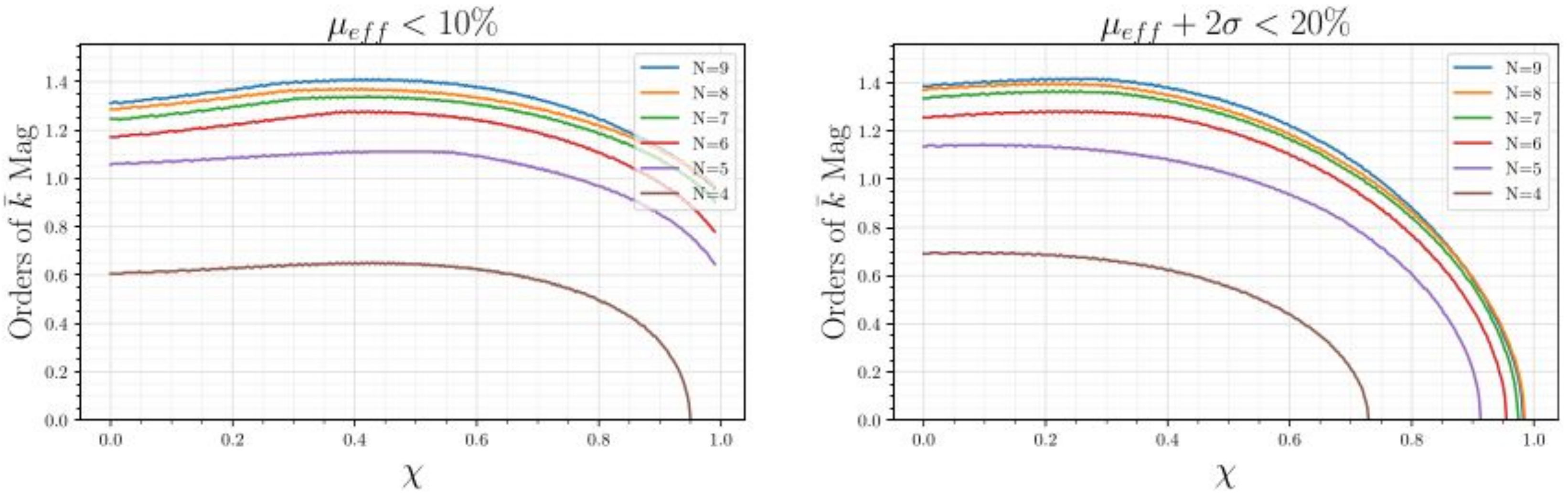

Figure 7. Using our equations of effective error μ_{eff} and σ, we plot how many orders of magnitude of wavevectors $\bar{k}$ can be reconstructed with two different measures of accuracy and precision. The left panel shows how many orders of $\bar{k}$ can be reconstructed such that μ_{eff} is less than 10%. The right panel shows how many orders of $\bar{k}$ can be reconstructed such that $\mu_{\text{eff}} + 2\sigma$ is less than 20%.

HelioSwarm Application

With 9 spacecraft, we have 128 tetrahedra, and 382 polyhedra with N>4, so let’s investigate the scales over which this observatory will be able to resolve k.